A Letter of Intent for a Neutrino Scattering Experiment Using an AGS Neutrino Beam

July 29, 2004

L. Bugel, J. M. Conrad, J. M. Link, M. H. Shaevitz, L. Wang, G. P. Zeller
Columbia University, Nevis Labs, Irvington, NY 10533

S. Brice, D. Finley
Fermi National Accelerator Laboratory, Batavia, IL 60510

J. C. Peng
University of Illinois at Urbana-Champaign, Urbana, IL 61801

J. Doskow, C. Horowitz, T. Katori, H. O. Meyer, R. Tayloe*, G. Visser
Indiana University, Bloomington, IN 47408

C. Green, G. T. Garvey, W. C. Louis, G. McGregor, H. Ray, R. Van de Water
Los Alamos National Laboratory, Los Alamos, NM 87545

R. Imlay, W. Metcalf, M. O. Wascko
Louisiana State University, Baton Rouge, LA 70803

V. Papavassiliou, S. F. Pate
New Mexico State University, Las Cruces, NM 88003

C. Dukes, L. Lu, K. Nelson, A. Norman
University of Virginia, Charlottesville, VA 22901

B. T. Fleming*
Yale University, New Haven, CT 06520

---

* Co-spokespersons: B. T. Fleming and R. Tayloe

Contents

1 Executive Summary **1**

2 Physics Motivation **3**

2.1 Δs Measurement 4

2.1.1 Δs: Strange Matrix Element of the Axial Current 5

2.1.2 Astrophysical Relevance of Δs 7

2.1.3 Current Information on Δs 9

2.1.4 Ongoing Experimental Programs Relevant to a Measurement of Δs 17

2.1.5 Combining νN and Parity-Violating $\vec{e}N$ Elastic Data 18

2.1.6 A BNL Measurement of Δs Using NC and CC νN Scattering 19

2.2 Neutrino Cross Sections 22

2.2.1 Motivation for Improved Cross Section Measurements 22

2.2.2 Present Understanding of Quasi-Elastic and Single Pion Cross Sections 24

2.2.3 Prospects for Measuring Cross Sections 25

3 The Neutrino Beam and Expected Event Rates **33**

3.1 The AGS Neutrino Beam 34

3.1.1 Protons from the AGS 34

3.1.2 The Neutrino Beamline 35

3.1.3 The Neutrino Flux 36
3.2 Neutrino Event Rates 37

4 The Detector **41**
4.1 Detector Overview 41
4.2 The Vertex Detector 42
4.2.1 Prototype Tests 45
4.3 The Muon Rangestack 46
4.4 Signal Readout: Phototubes and Electronics 47
4.5 A Possible Future Upgrade: Liquid Argon Time Projection Chamber 48
4.5.1 Detection Technique and Detector Construction 49
4.5.2 R&D program 50
4.6 Experimental Area at Brookhaven 50

5 Physics Sensitivity **53**
5.1 Introduction to Interactions in the Detector 53
5.2 Physics Simulations 59
5.2.1 Simulation of the Detector 59
5.2.2 Event Reconstruction 61
5.3 Physics Sensitivities 66
5.3.1 Δs Measurement 66
5.3.2 Neutrino Cross Section Measurements 70

6 Conclusions **77**

Bibliography **79**

Chapter 1

Executive Summary

The experiment described in this Letter of Intent provides a decisive measurement of Δs, the spin of the nucleon carried by strange quarks. This is crucial as, after more than thirty years of study, the spin contribution of strange quarks to the nucleon is still not understood.

Measurements from Deep Inelastic Scattering (DIS) experiments using charged leptons suffer from the fact that the missing spin can be due to the s quarks or to erroneous extrapolations of the data to an unmeasured kinematic region. It is also necessary for these experiments to assume SU(3) flavor symmetry. Furthermore, DIS experimental results from different techniques do not agree. What is required is a measurement which directly probes the spin of the strange quark.

Neutrino experiments provide a theoretically clean and robust method of determining Δs by comparing the neutral current interaction, which is isoscalar plus isovector, to the charged current interaction, which is strictly isovector. A past experiment, E734, performed at Brookhaven National Laboratory, has pioneered this effort. Building on what they have learned, we present an experiment which achieves a measurement to ± 0.04, which is better than past measurements and suffers from none of the theoretical ambiguities that plague DIS.

This experiment can also measure neutrino cross sections in the energy range required for accelerator-based precision oscillation measurements. Accurate measurements of cross sections have been identified as a priority of the neutrino community, as determined through the APS Multidisciplinary Study on the Future of Neutrino Physics. The experiment described here will provide unique information on cross

sections of $\sim$1 GeV neutrinos.

Brookhaven National Laboratory is a natural place to perform this experiment. The physics goals proposed here complement the existing BNL nuclear physics program. In addition, establishing a small neutrino program may benefit the very long term physics goals of the laboratory. The appropriate facilities are, to a large extent, already available on site. The very powerful AGS allows completion of the measurement in a short 4-month run, running concurrently with the RHIC program and prior to RSVP.

Our case is presented in the following order:

- Chapter 2 provides the physics motivation for these measurements, establishing that a new neutrino experiment is necessary;
- Chapter 3 describes the flux and event rates at this experiment produced by a new neutrino beamline at the Brookhaven AGS, justifying the request for a 4-month run;
- Chapter 4 sets forth detection techniques, demonstrating that an appropriate detector can be built on a reasonable time scale for \$2.8M, including contingency;
- Chapter 5 examines neutrino interactions in the detector for the physics measurements, showing that a decisive measurement can be achieved;
- Chapter 6 provides a summary and conclusion.

We intend to submit a formal proposal for this experiment to the Brookhaven Directorate in 2005.

Chapter 2

Physics Motivation

This experiment will cleanly measure the strange quark contribution to the nucleon spin, Δs, as well as a suite of neutrino cross sections in the crucial 1 GeV energy region.

The strange quark contribution to the nucleon spin remains unresolved after several decades of work via deep-inelastic scattering experiments. Neutrino neutral-current (NC) elastic scattering is uniquely sensitive to the nucleon axial structure and offers the best method for extracting Δs. Only one previous neutrino scattering experiment to date, BNL E734 [1], has attempted to measure Δs, albeit with limited precision and sensitivity. A next generation neutrino scattering experiment described here is crucial to cleanly determining Δs.

In addition to NC elastic scattering, this experiment can measure a full palette of neutrino interactions at low energy ($\approx$ 1 GeV). Cross section data on such reactions are sparse. Improved knowledge of low energy neutrino interaction rates on a nuclear target is becoming increasingly important as neutrino oscillation experiments in this energy range enter the precision era.

This chapter motivates these measurements, describing their history and presenting the improved precision and sensitivity this experiment can achieve.

2.1 Δs Measurement

From the time that the composite nature of the proton was discovered, physicists have sought to understand its constituents. The study of nucleon spin has grown into an industry, and opened new theoretical frontiers. Deep-Inelastic Scattering (DIS) measurements with polarized beams and/or targets have given us a direct measurement of the spins carried by the quarks in the nucleon. A central mystery has unfolded: in the nucleon, if the u and d valence quarks carry approximately equal and opposite spins, where lies the remainder?

One key contribution that has eluded a definitive explanation is the spin contribution from strange quarks in the nucleon sea. A large strange quark spin component, extracted from recent measurements [2], would be of great theoretical interest, since it would require significant changes to current assumptions. Is this large value of the strange spin due to chiral solitons [3], a misinterpretation of the large gluon contributions coming from the QCD axial anomaly [4, 5], or incorrect assumptions of SU(3) symmetry [6]? In addition, an understanding of the nucleon spin structure is a key input to dark matter searches and to the understanding of core collapse supernovae.

It has been known for some time that low energy (and low-Q^2) neutrino measurements are a theoretically robust technique (as robust as, e.g., the Bjorken sum rule) for isolating the strange quark contribution. Low-energy, intense neutrino beams now make it possible to take greater advantage of this method. The experiment described here, using these beams along with a novel detection technique, will resolve the presently murky experimental picture.

This experiment will measure Δs by examining neutral current neutrino-proton scattering; the rate of this process is sensitive to any contributions from strange quarks (both s and $\bar{s}$) to the nucleon spin. Specifically, Δs is extracted from the ratio of neutral current neutrino-proton ($\nu p \rightarrow \nu p$) scattering to charged current neutrino-neutron ($\nu n \rightarrow \mu^- p$) scattering. The measurement will be performed at low momentum transfer ($Q^2 \approx 0.2$ GeV^2), in order to unambiguously extract Δs from the axial form factor, G_A. We will improve on the latest measurement of neutral current neutrino-proton scattering (BNL 734) [1] by measuring this process not only at a lower-Q^2, but also with more events, less background, and lower systematic uncertainty.

In the following sections, we describe previous and current experiments relevant

to the question of strange quarks in the nucleon. We then describe why neutral current neutrino-nucleon elastic scattering is sensitive to the axial structure of the nucleon. We show a recent analysis of how the data may be analyzed together with PV electron scattering data. We conclude with a summary of the sensitivity of this experiment to Δs (detailed more completely in Chapter 5).

2.1.1 Δs: Strange Matrix Element of the Axial Current

In the current experimental program of nucleon structure studies, we find two broad areas of experimentation. First, elastic scattering of electrons from nucleons is used to measure the electroweak and axial form factors of the nucleon over a range of momentum transfer of $0.1 < Q^2 < 10$ GeV^2. These experiments have taken place at a variety of laboratories over the years, with the current program focused at MIT-Bates, JLab, and Mainz. The emphasis of the current program has been on determining the strange quark contributions to the electromagnetic form factors, through the exploitation of the interference between photon and Z-boson exchange processes. Second, deep-inelastic scattering of muons and electrons from nucleon and nuclear targets, historically responsible for the discovery of the partonic structure of matter, continues to play a role in the exploration of the distribution of quarks and gluons in nucleons. One of the highlights here is the focus, over the last 15 years, on the spin structure of the nucleon. The deep-inelastic exploration of nucleon spin takes place now at both leptonic and hadronic facilities — the spin program at RHIC being the most notable example of an hadronic facility taking on this physics topic.

QCD provides a simple framework in which these two experimental programs are joined together. The asymmetries observed in the polarized deep-inelastic scattering experiments arise from the antisymmetric part of the virtual Compton amplitude, which contains at its heart the nucleon axial current, $\bar{q}\gamma_\mu\gamma_5 q$. In the quark-parton model, inclusive scattering of leptons from nucleon targets measures the nucleon structure function F_1,

$$F_1(x) = \frac{1}{2}\sum_q e_q^2 q(x)$$

where e_q and $q(x)$ are respectively the charge and parton distribution function for quarks of flavor q. Inclusive scattering of **polarized** leptons from **polarized** nucleon targets measures the **spin-dependent** nucleon structure function g_1,

$$g_1(x) = \frac{1}{2}\sum_q e_q^2 \Delta q(x)$$

where now $\Delta q(x)$ is a polarized parton distribution function; it is defined as $\Delta q(x) = q^{\uparrow}(x) - q^{\downarrow}(x)$, where $q^{\uparrow}(x)$ and $q^{\downarrow}(x)$ are respectively the distributions for quarks to be found parallel or anti-parallel to the proton spin. In QCD, these distribution functions take on a scale dependence: $\Delta q(x, Q^2)$. At the same time, the axial form factors $G_A^q(Q^2)$ measured in elastic neutrino scattering are themselves matrix elements of the axial current,

$$_N\langle p'|\bar{q}\gamma_\mu\gamma_5 q|p\rangle_N = \bar{u}(p')\gamma_\mu\gamma_5 G_A^q(Q^2)u(p)$$

where the matrix element has been taken between two nucleon states of momenta p and p', and $Q^2 = -(p'-p)^2$. The diagonal matrix elements of the axial current are called the axial charges,

$$_N\langle p|\bar{q}\gamma_\mu\gamma_5 q|p\rangle_N = 2M s_\mu \Delta q$$

where M and s_μ are respectively the mass and spin vector of the nucleon. The quantities Δq are called "axial charges" because they are the value of the axial form factors at $Q^2 = 0$; that is to say, for example, $G_A^s(Q^2 = 0) = \Delta s$. The connection between the two sets of observables lies in a well-known QCD sum rule for the axial current, namely that the value of the axial form factor at $Q^2 = 0$ is equal to the integral over the polarized parton distribution function measured at $Q^2 = \infty$. For example,

$$\Delta s = G_A^s(Q^2 = 0) = \int_0^1 \Delta s(x, Q^2 = \infty)dx.$$

In this way, the axial charges Δq provide the link between the low-energy elastic neutrino scattering measurements of axial form factors and the high-energy deep-inelastic measurements of polarized parton distribution functions.

Of course, there are practical difficulties in the full exploration of this sum rule. No scattering experiment can reach $Q^2 = 0$ or $Q^2 = \infty$, and no deep-inelastic experiment can ever reach $x = 0$. However, the consequences of these difficulties are more severe in some cases than in others. The inability to reach $Q^2 = \infty$ in the deep-inelastic program means that QCD corrections enter into the sum rule written above. There is much theoretical experience in calculating these corrections. While the low-energy elastic experiments cannot reach $Q^2 = 0$, divergent behavior of the form factors near $Q^2 = 0$ is not expected and so the idea of extrapolating to $Q^2 = 0$ from measurements at low, non-zero Q^2 is not met with alarm. On the other hand, the limitations imposed by the inability to reach $x = 0$ in the deep-inelastic experiments are more problematic. The unpolarized parton distribution functions $q(x)$

are all known to increase rapidly as $x \to 0$ and there is no calculation of the expected behavior near $x = 0$ to rely upon for an extrapolation from measurements made at $x \neq 0$. Similar comments apply to the polarized parton distributions $\Delta q(x)$. Unpolarized measurements of the parton distributions at HERA have reached very low values of x, nearing $x = 3 \times 10^{-5}$, but the corresponding measurements of the polarized distribution functions, from data at SLAC, CERN, and DESY, only reach $x = 3 \times 10^{-3}$. Therefore, measurements of the axial charges place important constraints on the behavior of the distributions $\Delta q(x)$ in the unmeasurable low-x region.

As this Letter of Intent will demonstrate, the only way to measure the strange axial charge, Δs, is by means of low-energy elastic scattering of neutrinos from nucleons.

2.1.2 Astrophysical Relevance of Δs

Δs is a fundamental property of the nucleon that is not well-known and will lead to much insight into nucleon structure. In addition, it is a quantity that needs to be better measured to understand two important astrophysical questions.

Core Collapse Supernovae

Core collapse supernovae (SN) are massive explosions of single stars that are dominated by neutrinos and their weak interactions. Ninety-nine percent of the total energy released is radiated in neutrinos. The mean free path for μ and τ neutrinos is dominated by neutrino-nucleon elastic scattering. These neutrinos do not have enough energy for charged current interactions that require producing a charged lepton. The mean free path determines the diffusion time and indeed neutrinos were observed for about 10 seconds from SN1987A. The mean free path also determines the rate of energy transfer from the hot protoneutron star to matter near the shock front. This shock is thought to be energized by neutrino interactions and eventually ejects 90% of the star to form the supernova. Such calculations are very sensitive to the details of how neutrinos interact with matter. This is because there is so much more energy in the neutrino radiation and a small change in the energy deposition can determine if the shock succeeds in exploding the star or fails and the system collapses to a black hole. A number of theorists are presently performing large scale numerical simulations of SN, see, for example, Ref. [7].

Much of the matter behind the shock has been dissociated into nearly free nucleons that are mostly neutrons because of rapid electron capture. Therefore, one of the most important reactions is neutrino-neutron elastic scattering. In a SN, typical neutrino energies are near 25 MeV so momentum transfers are small. This cross section is still uncertain at the approximately 20% level because of the unknown value of the strange quark axial charge, Δs. The effect of strange quark uncertainties on neutrino opacities is discussed in Ref. [8]. The measurement described in this Letter will provide better input for such SN simulations. A smaller cross section would imply a smaller diffusion time and, other things being equal, a more rapid transport of energy from the protoneutron star to the region near the shock front.

Dark Matter Searches

Understanding the spin contribution to the nucleon of the strange quarks is important for certain searches of dark matter [9]. In R-parity-conserving supersymmetric models, the lightest supersymmetric particle (LSP) is stable and therefore a dark-matter candidate; in certain scenarios, the relic LSP density is large enough to be of cosmological interest. Experimental searches for cosmic LSPs can be competitive with accelerator-based searches [10].

In the case where the LSP is the neutralino, cosmic LSP can be detected either directly, through elastic neutralino scattering in an appropriate target/detector, or indirectly. The indirect method involves detecting high-energy neutrinos from neutralino annihilations in the center of the sun: neutralinos in the galactic halo can lose energy through elastic scattering with nuclei as they pass through the sun and become gravitationally trapped, sinking to the center. There, they accumulate and can subsequently annihilate into gauge bosons or heavy quarks; a significant fraction of the decay products of those involves high-energy neutrinos. The accumulation rate, and therefore the observed neutrino flux on earth, depends on the neutralino-nucleon scattering cross section (see [11] for a detailed calculation).

The neutralino-nucleus elastic-scattering cross section contains a spin-dependent and a spin-independent part. The spin-dependent part is given by

$$\sigma = \frac{32}{\pi} G_F^2 m_r^2 \Lambda^2 J(J+1),$$

where G_F is the Fermi constant, m_r the reduced neutralino mass, J the nucleus spin,

and

$$\Lambda \equiv \frac{1}{J}\left(a_p \left\langle S_p \right\rangle + a_n \left\langle S_n \right\rangle\right);$$

here $\left\langle S_{p(n)} \right\rangle$ is the average proton (neutron) spin in the nucleus and

$$a_{p(n)} = \sum_i \frac{\alpha_i}{\sqrt{2}G_F} \Delta q_i^{p(n)},$$

where the sum is over quark flavors and the coefficients α_i are functions of the composition of the neutralino in terms of the supersymmetric partners of the gauge bosons. The factors Δq_i^p and Δq_i^n are the quark contributions to the proton or neutron spin.

It is established [2, 12] that Δu and Δd have opposite signs. Therefore from the above, it should be clear that knowledge of Δs is not only important for the interpretation of any limits from such dark matter searches, but could also influence the choice of detector material for direct searches [13], making nuclei with either proton- or neutron-spin excess optimal, depending on its value and sign.

2.1.3 Current Information on Δs

The importance of measuring Δs has been known for quite some time, yet it is not an exaggeration to say this quantity has never been measured. All information to date on Δs is laden with questionable theoretical assumptions coupled to extrapolations of experimental data into unmeasured regions. In this section we show why a robust measurement of Δs is long overdue.

Δs from E734

The only extensive neutrino-nucleon elastic scattering data available are from the BNL E734 experiment [1]. This experimental program had many goals, one of which was the extraction of Δs. The experiment measured the cross sections for $\nu p \to \nu p$ and $\bar{\nu} p \to \bar{\nu} p$ elastic NC scattering in seven Q^2 bins over the kinematic range $0.45 < Q^2 < 1.05$ GeV^2. The cross sections were normalized [14] to the event rate for $\nu n \to \mu^- p$ and $\bar{\nu} p \to \mu^+ n$ quasi-elastic CC scattering, for which the cross sections were already known [15]. The error on these measured cross sections in the lowest Q^2 bin was 20% (22%) for the $\nu p \to \nu p$ ($\bar{\nu} p \to \bar{\nu} p$) reaction.

Elastic neutrino-nucleon scattering is very sensitive to the axial form factor of the nucleon. The cross section for νp and $\bar{\nu}p$ elastic scattering is given by [16]

$$\frac{d\sigma}{dQ^2} = \frac{G_F^2}{2\pi}\frac{Q^2}{E_\nu^2}(A \pm BW + CW^2)$$

where the $+$ $(-)$ sign is for ν $(\bar{\nu})$ scattering, and

$$\begin{aligned}
W &= 4(E_\nu/M_p - \tau) \\
\tau &= Q^2/4M_p^2 \\
A &= \frac{1}{4}\left[(G_A^Z)^2(1+\tau) - \left((F_1^Z)^2 - \tau(F_2^Z)^2\right)(1-\tau) + 4\tau F_1^Z F_2^Z\right] \\
B &= -\frac{1}{4}G_A^Z(F_1^Z + F_2^Z) \\
C &= \frac{1}{64\tau}\left[(G_A^Z)^2 + (F_1^Z)^2 + \tau(F_2^Z)^2\right].
\end{aligned}$$

Here, E_ν is the neutrino beam energy, and F_1^Z, F_2^Z, and G_A^Z are respectively the neutral weak Dirac, Pauli, and axial form factors. At low Q^2, this cross section is dominated by the axial contribution:

$$\frac{d\sigma}{dQ^2}(Q^2=0) = \frac{G_F^2}{128\pi}\frac{M_p^2}{E_\nu^2}\left[(-\Delta u + \Delta d + \Delta s)^2 + (1 - 4\sin^2\theta_W)^2\right].$$

The quantity $\Delta u - \Delta d$ is already known from neutron β decay; this is just g_A, the $Q^2 = 0$ value of the CC part of the axial form factor. So, the only unknown part is the strange axial charge, Δs. Of course, the measurement cannot be performed at $Q^2 = 0$ so a determination of Δs will always involve an extrapolation over some unmeasured interval near $Q^2 = 0$.

In their Δs analysis the E734 collaboration use a dipole form for the weak axial form factor,

$$G_A^Z(Q^2) = \frac{1}{2}\frac{g_A(1+\eta)}{(1+Q^2/M_A^2)^2}$$

where $g_A = 1.26$ is the CC coupling constant measured in neutron β decay, M_A is the "axial mass" parameter used in fitting the Q^2-dependence of the known (CC) part of the axial form factor, and η is a parameter used to measure the size of strange quark contributions to the axial form factor. In our modern notation, $\Delta s = -\eta g_A$. It is important to note that while the dipole shape fits the CC part of the axial form factor nicely, this form has no physical significance and there is no theoretical support for the idea that the strange sea contribution to the form factor should have

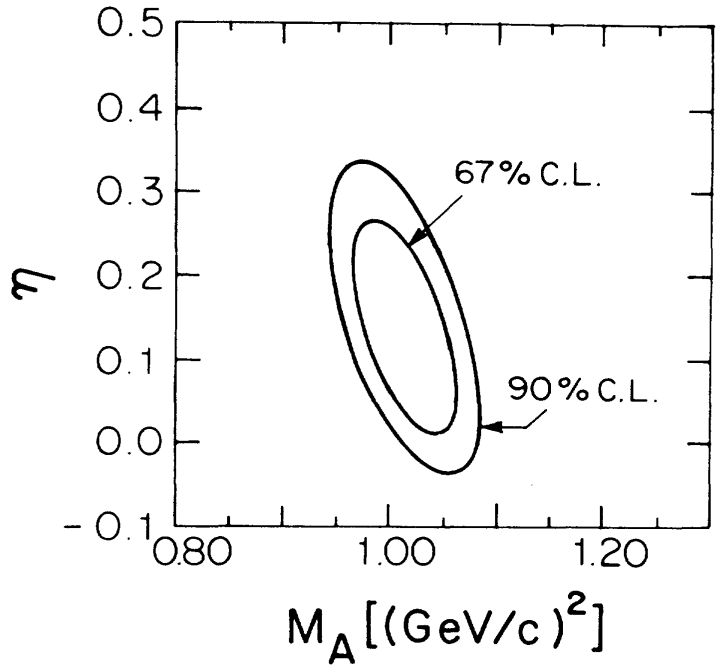

Figure 2.1: Results from a fit of the BNL E734 $\nu p \to \nu p$ and $\bar{\nu} p \to \bar{\nu} p$ scattering data [1] indicating the preferred values of η $(= -\Delta s/g_A)$ and M_A. (Figure from Ref. [1].)

the same Q^2-dependence as the up- and down-quark valence contribution. Fitting their data to extract η, with M_A at the world average at that time, they found a value $\eta = 0.12 \pm 0.07$, implying a value of $\Delta s = -0.15 \pm 0.09$. A simultaneous fit to both η and M_A yields a value of η with a substantially larger error as may be seen from the fit results, shown in Figure 2.1. The current world average neutrino scattering data give $M_A = 1.026 \pm 0.021$ [17].

Many years later, Garvey, Louis and White [16] performed a reanalysis of the E734 data introducing a number of additional features, compared to the original E734 analysis:

- Allowed for non-zero values of the vector strange form factors, which had been set to zero in the E734 analysis.
- Introduced a floating normalization for each data point, to allow for the uncertainty in the nuclear corrections made in the E734 cross section extraction procedure.

- Included more recent nucleon form factor values, while continuing to assume the strange and non-strange axial form factors shared the same dipole form with the same parameter M_A.

Even with these improvements, this analysis resulted in a measurement of Δs with large errors due the limited precision of the E734 data and the large uncertainty arising from the extrapolation to $Q^2 = 0$. The results from a simultaneous fit of Δs, the two strange vector form factors, (F_1^s and F_2^s), and constraining M_A to the world-average at that time, yielded $\Delta s = -0.21 \pm 0.10$. However, satisfactory fits were obtained for Δs ranging from 0 to -0.21 depending on the details of the Q^2 evolution of the axial form factor.

More recently, Alberico *et al.* [18] performed a rather different analysis using the E734 data, again with the goal of extracting the strange form factors of the proton. Instead of a point-to-point analysis and fit of the data, they focused their attention upon the use of several integral ratios reported by E734, namely

$$R_\nu = \frac{\langle\sigma\rangle_{\nu p\to\nu p}}{\langle\sigma\rangle_{\nu n\to\mu^- p}} = 0.152 \pm 0.007(\text{stat}) \pm 0.017(\text{syst})$$

$$R_{\bar\nu} = \frac{\langle\sigma\rangle_{\bar\nu p\to\bar\nu p}}{\langle\sigma\rangle_{\bar\nu p\to\mu^+ n}} = 0.218 \pm 0.012(\text{stat}) \pm 0.023(\text{syst})$$

$$R_{\nu/\bar\nu} = \frac{\langle\sigma\rangle_{\nu p\to\nu p}}{\langle\sigma\rangle_{\bar\nu p\to\bar\nu p}} = 0.302 \pm 0.019(\text{stat}) \pm 0.037(\text{syst})$$

where each $\langle\sigma\rangle$ is an average over the range $0.5 < Q^2 < 1.0$ GeV^2. These three ratios are then combined into a single ratio,

$$\langle A_p\rangle = \frac{\langle\sigma\rangle_{\nu p\to\nu p} - \langle\sigma\rangle_{\bar\nu p\to\bar\nu p}}{\langle\sigma\rangle_{\nu n\to\mu^- p} - \langle\sigma\rangle_{\bar\nu p\to\mu^+ n}} = \frac{R_\nu(1 - R_{\nu/\bar\nu})}{1 - R_{\nu/\bar\nu}R_\nu/R_{\bar\nu}}.$$

This ratio method allows for cancellation of any multiplicative errors associated with nuclear effects in the extraction of the original cross sections in E734. While this analysis pointed out the power of ratios in reducing nuclear model uncertainties, the errors on the E734 data did not allow a precise extraction of Δs and the conclusions were consistent with the Garvey, Louis, White reanalysis of the data described above [16], yet led to no additional insight on the value of Δs.

As is evident in this discussion, the BNL E734 data has generated a large amount of interest; this points to growing appreciation of the fact that neutral current neutrino scattering is an excellent probe of Δs. Unfortunately, however, the BNL E734 data cannot determine Δs.

Δs from Charged-Lepton Deep-inelastic Scattering

As mentioned earlier, the double-spin asymmetries in polarized inclusive leptonic deep-inelastic scattering measure the spin-dependent nucleon structure function g_1:

$$g_1(x) = \frac{1}{2}\sum_q e_q^2 \Delta q(x).$$

In leading order QCD, these functions take on a scale dependence:

$$g_1(x, Q^2) = \frac{1}{2}\sum_q e_q^2 \Delta q(x, Q^2).$$

In next-to-leading order (NLO) QCD, there are significant radiative corrections and the relation between g_1 and the Δq becomes more complex. In the discussion here, we limit our attention to the leading-order QCD analysis because the NLO version of the analysis does not change the result (nor the uncertainty) for Δs very much, and the problems to be pointed out exist at all orders, because they are problems stemming from the data itself.

Consider the analysis from the SMC Collaboration [12] as an example. They measured $g_1(x, Q^2)$ over a wide kinematic range, $0.003 < x < 0.70$ and $1.3 < Q^2 < 58.0$ GeV^2. This coverage is not a rectangle, *i.e.* there is a correlation between x and Q^2 in the acceptance of the experiment, and so for a reasonable analysis it is necessary to use QCD to evolve all the data to a single value of Q^2, in this case $Q^2 = 10$ GeV^2. In the process of performing this evolution, a fit function for g_1 is produced. Then, to integrate the distribution g_1 over $0 < x < 1$, it is necessary to extrapolate to $x = 1$ and $x = 0$. The extrapolation to $x = 1$ makes use of the fact that g_1, being a difference of two quark distributions, must go to 0 as $x \to 1$. This requirement is satisfied by assuming the measured experimental asymmetry to be constant for $x > 0.7$. The extrapolation to $x = 0$, on the other hand, is not straightforward, as the expected behavior of $g_1(x)$ for $x \to 0$ is unknown. In this analysis, two methods were used. In one, the QCD evolution fit was simply extrapolated to $x = 0$. In another, called the "Regge extrapolation," the value of g_1 was assumed to be constant for $x < 0.003$. The results of these extrapolations may be seen in Fig. 2.2. The two values of the integral of g_1 from these extrapolations are

$$\begin{aligned} \Gamma_1 = \int_0^1 g_1(x)dx &= 0.142 \pm 0.017 \quad \text{“Regge”} \\ &= 0.130 \pm 0.017 \quad \text{QCD fit.} \end{aligned}$$

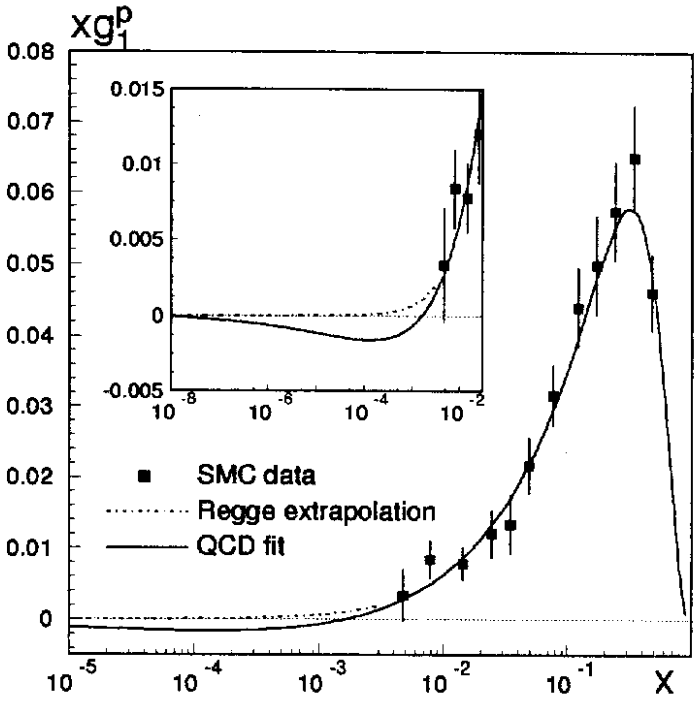

Figure 2.2: Results of the SMC measurements of $g_1(x, Q^2)$. Plotted is xg_1 as a function of x. The QCD fit is the continuous line, while the extrapolation assuming Regge behavior is indicated by the dot-dashed line. The inset is a close-up extending to lower values of x. (Figure from Ref. [12].)

This integral is related to the axial charges:

$$\Gamma_1 = \int_0^1 g_1(x)dx = \frac{1}{2}\sum_q e_q^2 \int_0^1 \Delta q(x)dx = \frac{1}{2}\left[\frac{4}{9}\Delta u + \frac{1}{9}\Delta d + \frac{1}{9}\Delta s\right].$$

Now, assuming that SU(3)$_f$ is a valid symmetry of the baryon octet, and using hyperon β decay data, then two other relations between the three axial charges are determined:

$$\Delta u - \Delta d = g_A = F + D \qquad \text{and} \qquad \Delta u + \Delta d - 2\Delta s = 3F - D$$

where $g_A = 1.2601 \pm 0.0025$ and $F/D = 0.575 \pm 0.016$ (in 1997). Now one may solve for the axial charges, yielding the results shown in Table 2.1. Of course, the error bars quoted here do not include any estimate of the theoretical uncertainty underlying the assumption of SU(3)$_f$ symmetry. They do include an estimate of the uncertainty

Table 2.1: Results for the axial charges from the SMC analysis [12] of their inclusive DIS data.

	"Regge"	QCD fit
Δu	0.84 ± 0.06	0.80 ± 0.06
Δd	-0.42 ± 0.06	-0.46 ± 0.06
Δs	-0.08 ± 0.06	-0.12 ± 0.06

due to the extrapolations, but of course that is only an estimate because the actual behavior of g_1 is unknown in the $x \to 0$ region. The only conclusion to be drawn for Δs from this analysis is that it may be negative, with a value anywhere in the range from 0 to -0.2.

$\Delta s(x)$ from Semi-inclusive Leptonic Deep-inelastic Scattering

In semi-inclusive deep-inelastic scattering, a leading hadron is observed in coincidence with the scattered lepton. This allows a statistical identification of the struck quark, and hence a measurement of the x-dependence of the individual $\Delta q(x)$ distributions. (Inclusive scattering only measures the total structure function $g_1(x)$.) The HERMES Experiment [19] on the HERA ring at DESY was especially designed to make this measurement. HERMES measured double-spin asymmetries in the production of charged hadrons in polarized deep-inelastic scattering of positrons from polarized targets; specifically, the asymmetry in the production of charged pions on targets of hydrogen and deuterium, and of charged kaons in scattering from deuterium. There is no assumption of $\mathrm{SU}(3)_f$ symmetry in their analysis. They extract the following quark polarization distributions, over the range $0.023 < x < 0.30$ [20]:

$$\frac{\Delta u}{u}(x) \quad \frac{\Delta d}{d}(x) \quad \frac{\Delta \bar{u}}{\bar{u}}(x) \quad \frac{\Delta \bar{d}}{\bar{d}}(x) \quad \frac{\Delta s}{s}(x)$$

where $\frac{\Delta s}{s}(x)$ is defined to be the sum of $\frac{\Delta s}{s}(x)$ and $\frac{\Delta \bar{s}}{\bar{s}}(x)$. The results are shown in Fig. 2.3.

It is seen that within the measured uncertainties, and within the measured x-region, the valence quarks (u and d) are polarized and the sea quarks ($\bar{u}$, $\bar{d}$, and s) are unpolarized. The integral value of the measured polarized strange quark distribution

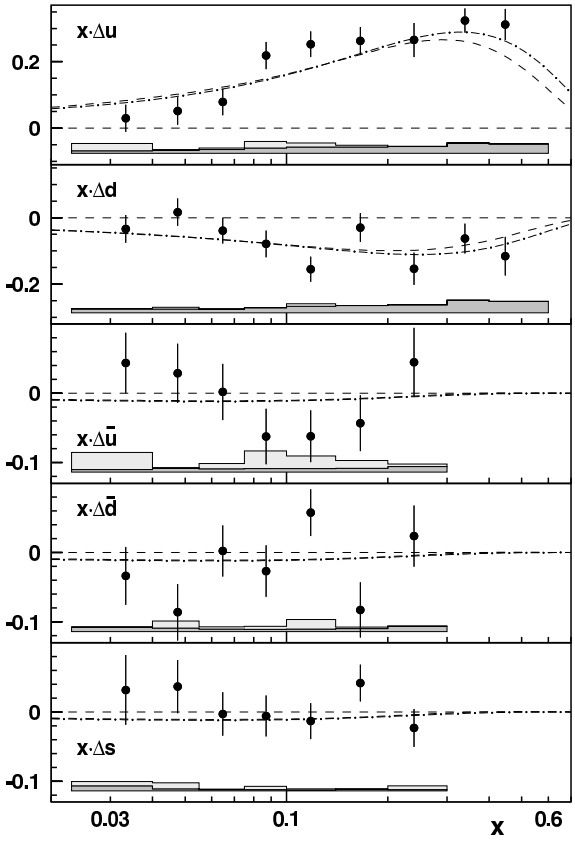

Figure 2.3: HERMES results for polarized parton distribution functions. (Figure from Ref. [20].)

is

$$\text{“}\Delta s\text{”} = \int_{x=0.023}^{0.30} \Delta s(x)dx = +0.03 \pm 0.03(\text{stat}) \pm 0.01(\text{syst}).$$

Note this would only be the true Δs if the integral was over the full range, $0 < x < 1$.

Given the fact that the inclusive analysis described in the previous section produced a negative value of Δs, it is natural to ask “where did the negative Δs go?” If the analyses of the inclusive and semi-inclusive data are both correct, then all the negative contribution to the value of Δs must come from the unmeasured x-region, that is from $x < 0.023$. That would imply an average value of $\Delta s(x)$ of approximately -5 in the range $x < 0.023$, which is not impossible, as $s(x)$ is of order 20-300 in the range $0.01 < x < 0.001$ [21]. Some very interesting physics indeed would be revealed, if the “turn on” of the strange quark polarization in the low-x region was this dramatic.

Of course, there are other explanations. The invocation of $SU(3)_f$ symmetry in the analysis of the inclusive data is known to be problematic and the extrapolations to $x = 0$ in those analyses do not have firm theoretical support. It is clear that a *direct* measurement of Δs would serve to clarify these issues.

2.1.4 Ongoing Experimental Programs Relevant to a Measurement of Δs

Parity-violating $\vec{e}N$ Elastic Scattering

One of the highlights of the current low- and medium-energy electron scattering program is the measurement of the strange vector form factors of the nucleon via parity-violating $\vec{e}N$ scattering. These measurements are sensitive as well to the non-strange part of the axial form factor, but rather insensitive to the strange axial form factor due to the relative sizes of kinematic factors multiplying the various form factors that contribute to the asymmetry. To be specific, the parity-violating asymmetry observed in these experiments, when the target is a proton, can be expressed as [22]

$$A_p = \left[\frac{-G_F Q^2}{4\pi\alpha\sqrt{2}}\right] \frac{\epsilon G_E^\gamma G_E^Z + \tau G_M^\gamma G_M^Z - (1-4\sin^2\theta_W)\epsilon' G_M^\gamma G_A^e}{\epsilon\left(G_E^\gamma\right)^2 + \tau\left(G_M^\gamma\right)^2}$$

where $G_{E(M)}^\gamma$ are the traditional electric (magnetic) form factors of the proton and $G_{E(M)}^Z$ are their weak (Z-exchange) analogs, $\tau = Q^2/4M_p^2$, M_p is the mass of the proton, $\epsilon = [1 + 2(1+\tau)\tan^2(\theta/2)]^{-1}$, θ is the electron scattering angle, and $\epsilon' = \sqrt{\tau(1+\tau)(1-\epsilon^2)}$. Lastly, G_A^e is the effective axial form factor seen in electron scattering:

$$G_A^e = -G_A^{CC}(1 + R_A^{T=1}) + G_A^s + R_A^{T=0}.$$

Here, G_A^{CC} is the non-strange (CC) axial form factor, G_A^s is the strange axial form factor, and the terms $R_A^{T=0,1}$ represent electroweak radiative corrections [22, 23, 24, 25]. The presence of these radiative corrections clouds the interpretation of the axial term extracted from these experiments. To solve this problem, the SAMPLE [26] experiment also measured the same asymmetry on a deuterium target, in which case the relative kinematic factors of the non-strange ($T = 1$) and strange ($T = 0$) parts of the axial form factor are changed, allowing a separation of the two. However, one may show that this does not help in identifying the value of G_A^s, because the relative

size of the kinematic factors for G_M^s and G_A^s remain the same for either target:

$$\frac{\partial G_M^s}{\partial G_A^s} = -(1 - 4\sin^2\theta_W)\frac{\epsilon'}{\tau} \approx -\frac{1}{2} \text{ for SAMPLE.}$$

Therefore, parity-violating $\vec{e}N$ scattering experiments can only establish a relationship between the strange magnetic and axial form factors, they cannot measure them separately.

Polarized Deep-Inelastic Scattering

The only two deep-inelastic experiments currently running or planned that will have anything to say about $\Delta s(x)$ are HERMES and the new COMPASS Experiment at CERN.

At HERMES, it would be possible to separately measure $\Delta s(x)$ and $\Delta\bar{s}(x)$ (instead of the lumped s and $\bar{s}$ distribution in the present set of results) if the asymmetry in the production of kaons from hydrogen (and not just deuterium) is also measured. However, it does not seem that this measurement will be done soon (if ever).

The COMPASS Experiment [27], while for the most part focused on a measurement of the gluon polarization, is also equipped to measure the distributions $\Delta s(x)$ and $\Delta\bar{s}(x)$ down to $x = 5 \times 10^{-3}$ with the same size of uncertainties as HERMES was able to achieve down to $x = 0.023$ (see Fig. 2.3). This will be a very interesting measurement, but of course it will not be able to establish the value of the axial charge, for the usual reason that the extrapolation to $x = 0$ contains too many uncertainties. As stated earlier, these sorts of deep-inelastic measurements are complementary to the strange axial charge measurement proposed in this Letter.

2.1.5 Combining νN and Parity-Violating $\vec{e}N$ Elastic Data

A third re-analysis of the BNL734 data by Pate [28] combines low energy νN data and parity violating $\vec{e}N$ elastic scattering data from HAPPEX [29]. Using the known values for the electric, magnetic, and non-strange (CC) axial form factors of the proton and neutron, the difference of the νp and $\bar{\nu}p$ elastic cross sections is taken and shown to be a function only of the strange magnetic and axial form factors, G_M^s and G_A^s. At the same time, the sum of the νp and $\bar{\nu}p$ elastic cross sections is shown to be a function only of the strange electric and magnetic form factors, G_E^s and

G_M^s. Measurements of forward-angle parity-violating $\vec{e}p$ elastic scattering are shown to be largely functions only of G_E^s and G_M^s as well. This re-analysis uses these three combinations of data to determine all three strange form factors. This results in two possible solutions at $Q^2 = 0.5$ GeV^2 summarized in Table 2.2 where Solution 1 is favored [28]. At the present time, there is only sufficient data at $Q^2 = 0.5$ GeV^2 to make such a determination.

Data from the G^0 Experiment [30], recently collected and in the process of analysis, will provide additional measurements of G_E^s and G_M^s in the range $0.5 < Q^2 < 1.0$ GeV^2 and will allow for the extraction of G_A^s from the E734 data. However, knowledge of the strange axial form factor over the range $0.5 < Q^2 < 1.0$ GeV^2 will not be sufficient for the extrapolation to $Q^2 = 0$ needed for a determination of Δs. New and more precise neutrino data at lower Q^2 are crucial for a definitive measurement.

Table 2.2: Two solutions for the strange form factors at $Q^2 = 0.5$ GeV^2 produced from the E734 and HAPPEX data. (Table from Ref. [28].)

	Solution 1	Solution 2
G_E^s	0.02 ± 0.09	0.37 ± 0.04
G_M^s	0.00 ± 0.21	-0.87 ± 0.11
G_A^s	-0.09 ± 0.05	0.28 ± 0.10

2.1.6 A BNL Measurement of Δs Using NC and CC νN Scattering

To address this need for a quality measurement of Δs, this Letter proposes to measure the NC to CC neutrino scattering ratio $R_{NC/CC} = \frac{\sigma(\nu p \to \nu p)}{\sigma(\nu n \to \mu^- p)}$ and from it extract the strange axial form factor down to $Q^2 = 0.2$ GeV^2. The numerator in this ratio is sensitive to the full axial form factor, $-G_A^{CC} + G_A^s$, while the denominator is sensitive to only G_A^{CC}. While the numerator maintains all the dependence on the strange axial form factor, measurement of the ratio reduces systematic uncertainties in neutrino flux, detector efficiency, nuclear target effects, and form factors.

The sensitivity of the NC elastic cross section and $R_{NC/CC}$ to G_A^s is shown in Figure 2.4 as a function of Q^2. Note how the NC differential cross section depends

strongly on G_A^s. This strong dependence of $R_{NC/CC}$ on G_A^s is shown explicitly in Figure 2.5 for three Q^2 bins. From this Figure, it can be seen that a 5% relative measurement of $R_{NC/CC}$ at $Q^2 \approx 0.25$ GeV^2 would enable an extraction of Δs with an error of ± 0.04.

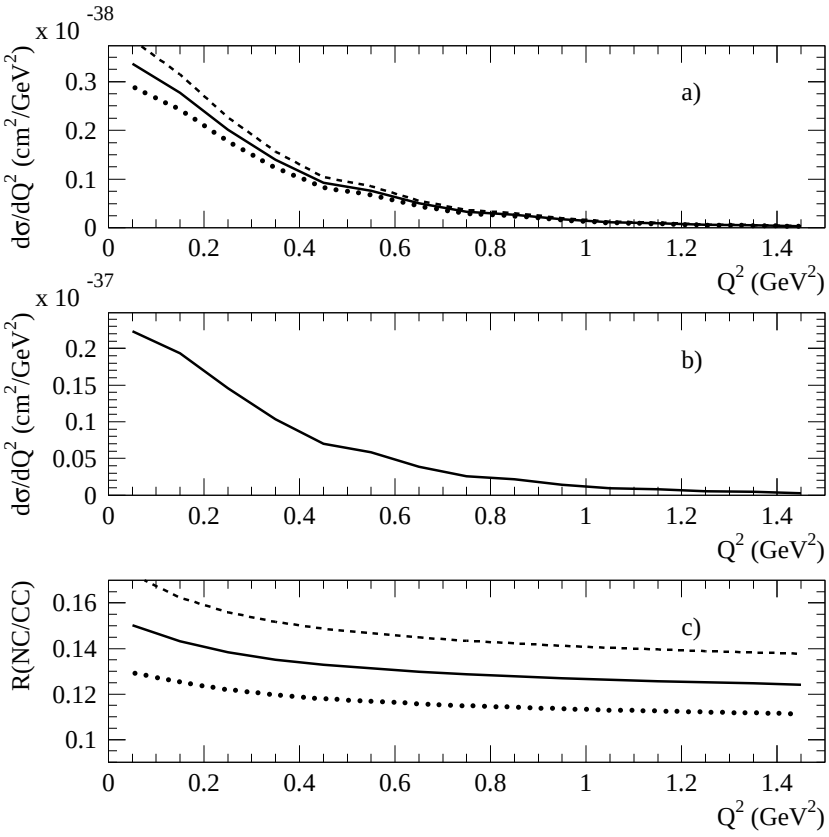

Figure 2.4: Flux-weighted differential cross section as a function of Q^2 for $\nu p \to \nu p$ (a) and $\nu n \to \mu^- p$ (b) scattering together with the cross section ratio of the these two processes (c). These quantities are shown for $G_A^s = 0.$ (solid), $= -0.1$ (dashed), and $= +0.1$ (dotted). The $\nu n \to \mu^- p$ process does not depend upon G_A^s.

In the actual measurement, all of the data in a range of Q^2 will be used to extract Δs and, of course, in an actual measurement, additional sources of error demand consideration. These have been studied and quantified as will be shown in Chapter 5. However, the added range in Q^2 ($Q^2 = 0.2 - 1.0$ GeV^2) and improved statistics offset these additional sources of error, resulting in a measurement of $R_{NC/CC}$, as described in this letter, to 5% allowing for a ± 0.04 measurement of Δs assuming minimal neutron identification capability.

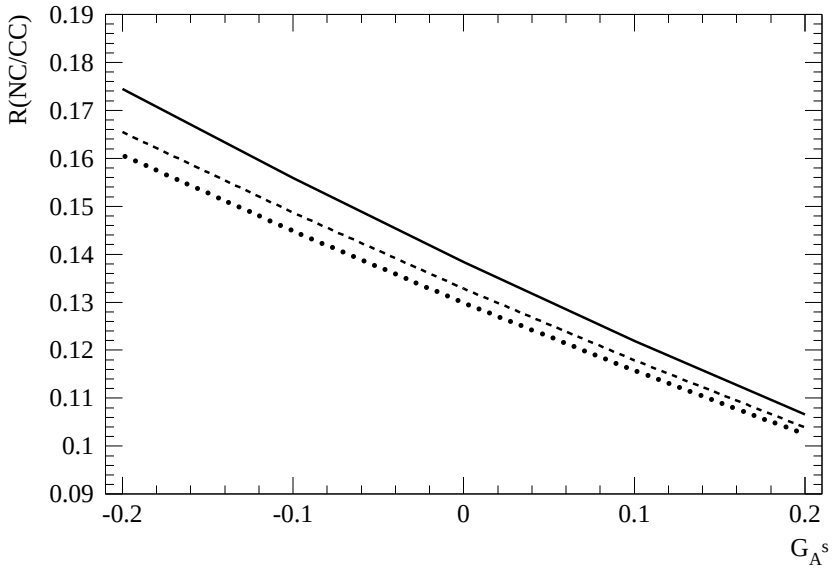

Figure 2.5: Ratio of flux-weighted cross sections of the $\nu p \to \nu p$ and $\nu n \to \mu^- p$ processes as a function of the axial form factor G_A^s at $Q^2 = 0.25$ (solid), 0.45 (dashed), and 0.65 (dotted) GeV^2.

With additional neutron background rejection, a significant reduction by perhaps as much as a factor of 2, will be possible. These studies are underway. This will be presented in the full proposal.

Building on past experience, this measurement will improve on the results of BNL E734, the best neutrino-nucleon elastic scattering measurement to date, in the following ways:

- Collecting an order of magnitude more data to reduce the statistical errors.
- Performing the measurement at a lower Q^2 which reduces the systematic uncertainty in Δs in extrapolating to $Q^2 = 0$.
- Reducing the background from other neutrino scattering processes. This reduces the systematic error on $R_{NC/CC}$.
- Designing the detector from the onset with the goal of measuring the NC to CC ratio. This will naturally allow for additional systematic error reductions in detector efficiencies.

The quoted expected sensitivity of ± 0.04 is conservative. With improved background rejection, this error can be reduced. But even these conservative errors are competive with the claims from the DIS experiments and the result is better in a number of ways:

- This method does not rely on assumptions of SU(3) flavor symmetry like those used in the extraction of Δs in the DIS experiments;
- The identity used in this analysis relating Δs and G_A^s is deeply fundamental, even as robust as the Bjorken Sum Rule.

Therefore, the experiment described in the Letter will provide the definitive statement on Δs.

2.2 Neutrino Cross Sections

Reliable measurement of CC and NC neutrino cross sections at low energy ($0.1 < E_\nu < 2$ GeV) where the existing data are sparse to nonexistent, would be of great theoretical and practical value. From a practical standpoint, a quantitative understanding of these reactions is critical for both present and future neutrino oscillation experiments. In particular, improved cross section measurements would provide valuable input to atmospheric and accelerator-based neutrino oscillation searches which probe these same energies in order to reach their maximum sensitivity. From a theoretical standpoint, neutrino interactions on nuclear targets (having only been marginally studied in the past) would allow greater insight into nuclear dynamics, shadowing, and coherent pion production processes.

The motivation for measuring low energy neutrino cross sections is described here, while the sensitivity of our apparatus to these processes is outlined in Chapter 5.

2.2.1 Motivation for Improved Cross Section Measurements

Current oscillation experiments model neutrino interactions in a regime that is poorly constrained by experimental data. Although accelerator-based neutrino beams have existed for over three decades, our primary knowledge of neutrino interactions at low energy comes almost entirely from bubble chamber measurements made decades

ago at ANL, BNL, CERN, and FNAL, all of which were limited by low statistics and large neutrino flux systematics. In addition to these large uncertainties of typically $10-40\%$, the experimental results often conflict and are difficult to interpret, mainly because of complications due to nuclear corrections and exclusive final state ambiguities. These data, while not as precise as DIS measurements, nonetheless are what presently constrain the Monte Carlo predictions used by many running neutrino experiments.

Improved knowledge of low energy neutrino cross sections will become increasingly important as experiments move from discovery to precision measurements of oscillation parameters. Consider the following examples:

- Present atmospheric constraints on Δm^2_{23} and θ_{23} are already limited by flux and cross section systematics.
- Uncertainties on NC π^0 production cross sections currently restrict the ability to discriminate between $\nu_\mu \to \nu_\tau$ and $\nu_\mu \to \nu_s$ transitions in studies of enriched NC samples in atmospheric neutrino data.
- $\nu_\mu \to \nu_e$ appearance searches are limited by statistical and systematic errors related to background subtraction, most notably those associated with NC π^0 interactions where the final state photoconversion is mis-identified as an electron. Both the kinematics and rate of NC π^0 production are less precisely known than most other reaction channels, because of the need to model resonant and coherent contributions in addition to potential feed-down from inelastic channels.
- ν_μ disappearance measurements could profit from improved knowledge on both QE interactions on nuclear targets and CC single π^+ production backgrounds.

More precise cross section measurements are not only important for ensuring the success of neutrino oscillation measurements, but are uniquely relevant for other searches. Resonant cross sections are a necessary input to $p \to \nu K^+$ proton decay searches, because poorly measured atmospheric neutrino interactions such as $\nu_\mu\, n \to \mu^-\, K^+\, \Lambda$ and $\nu_\mu\, p \to \nu_\mu\, K^+ \Lambda$ present significant backgrounds and hence large resultant systematics. In these regards, both present and future neutrino experiments could clearly benefit from improved knowledge of low energy neutrino cross sections.

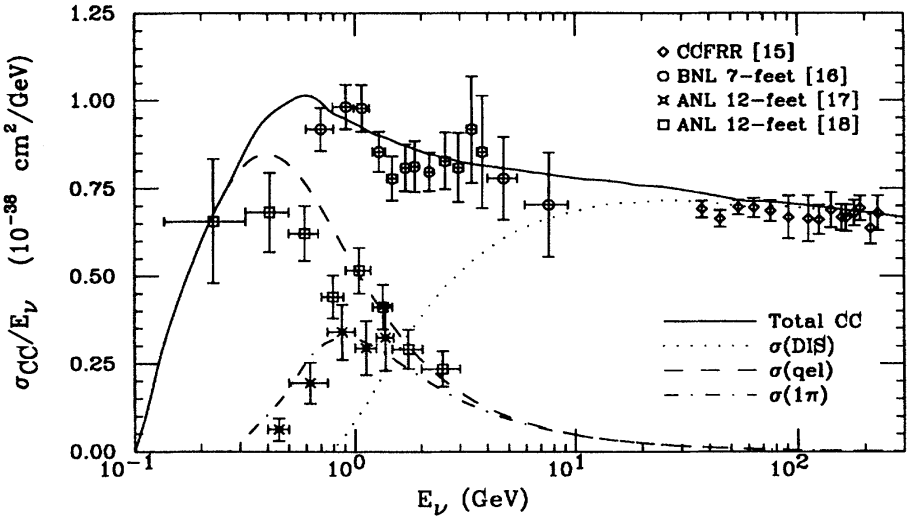

Figure 2.6: Charged current neutrino cross section contributions for an isoscalar target as a function of neutrino energy: quasi-elastic (dashed), resonant single pion (dot-dash), and deep inelastic scattering (dotted) processes. From [31].

2.2.2 Present Understanding of Quasi-Elastic and Single Pion Cross Sections

Figure 2.6 shows the contributing neutrino cross sections in the region of interest for atmospheric and terrestrial based neutrino oscillation experiments. At energies near $\sim$ 1 GeV, neutrino interactions include quasi-elastic (QE), resonant single pion, coherent single pion, and deep inelastic scattering (DIS) processes. Although DIS interactions have been measured with impressive precision ($< 2\%$) at high energies, the cross sections of the various contributing processes at low energy are much less well-known (typically to $10 - 40\%$) and largely come from light target (H_2, D_2) neutrino bubble chamber data. It is particularly challenging to measure and model neutrino interactions at low energies where there is substantial overlap between these various poorly-understood contributing processes. In this regard, the low energy regime is truly unique. The ability to successfully disentangle the various channels (QE, resonance, coherent, DIS, etc.) necessitates use of a fine-grained detector such as that being proposed here.

In contrast to many of these early low energy neutrino experiments, modern neutrino oscillation detectors employ heavy nuclear targets (C, O, Ar, Fe, Pb) in order to achieve their desired event rates. Complex targets add additional complications,

such as the effects of Pauli blocking, Fermi motion of the target nucleons, and final state interactions (i.e. careful accounting for the fact that the outgoing hadron may re-interact before exiting the target nucleus). Final state effects (nuclear re-interactions, π absorption, and charge exchange) often dominate; they can vary depending on the neutrino process, and their contributions certainly have not been disentangled experimentally. Nuclear effects significantly impact both the rate and kinematics of the neutrino reaction, as well as the observed final state event composition and multiplicity. Although nuclear effects have been studied extensively using muon and electron beams, no comparable effort has been made using neutrinos. Neutrino cross sections have been measured on nuclear targets in the past[1], but these experiments suffered from low statistics and typically published only free nucleon cross sections. By making dedicated, high statistics measurements of neutrino interaction cross sections on a scintillator-based target, this high precision, high statistics experiment could greatly improve the current experimental situation.

Several efforts are already underway to more precisely measure neutrino interactions on nuclei at low energy. Measurements of NC π^0/QE and inelastic/QE event ratios have been recently performed in the K2K water Čerenkov and scintillator-based fine grain near detectors [32]. These measurements exhibit $\sim$ 10% accuracy based on samples of roughly 5,000-10,000 events [33]. MiniBooNE can additionally offer improved cross section constraints, with increased statistics over the K2K near detector ensemble. Such Čerenkov-based detection methods are nonetheless inherently limited in their capabilities. The rest of this section highlights the value of large event samples combined with fine-grained detection.

2.2.3 Prospects for Measuring Cross Sections

The following subsections outline prospects for several exclusive neutrino cross section measurements. This includes improved constraints on NC π^0 production which would help improve the sensitivity of neutrino oscillation experiments looking for ν_e appearance, and strange particle production which is most relevant for GUT-favored proton decay searches.

[1] Gargamelle ($C_3H_8CF_3Br$), SKAT ($C_3H_8CF_3Br$), FNAL (Ne), CHARM and CHARM II (marble, glass), and Serpukhov (Al) are several examples.

Neutral Current π^0 Production

The dominant backgrounds to $\nu_\mu \to \nu_e$ appearance searches result from two principal sources: the intrinsic ν_e component in the beam and NC π^0 production where the final state photoconversion is misclassified as an electron. Current experiments rely almost entirely on Monte Carlo simulations to estimate their π^0 backgrounds. Such simulations must model several mechanisms for producing a single π^0: resonant and non-resonant production, coherent single pion production, and deep inelastic scattering in which additional hadrons are absorbed in the nuclear medium before being detected. The dominant means of single pion production at low energy arises through this first production mechanism: excitation of baryon resonances (Δ, N) that decay as:

$$\begin{aligned} \nu_\mu N \to l \quad & N^* \\ & N^* \quad \to \pi N' \ . \end{aligned}$$

As a result, there are seven such resonant neutrino reaction channels: three charged current and four neutral current:

$$\begin{aligned} \nu_\mu p &\to \mu^- p \pi^+ \\ \nu_\mu n &\to \mu^- n \pi^+ \\ \nu_\mu n &\to \mu^- p \pi^0 \end{aligned} \qquad \begin{aligned} \nu_\mu p &\to \nu_\mu n \pi^+ \\ \nu_\mu p &\to \nu_\mu p \pi^0 \\ \nu_\mu n &\to \nu_\mu n \pi^0 \\ \nu_\mu n &\to \nu_\mu p \pi^- \end{aligned}$$

Traditionally, Monte Carlo simulations covering the low energy region have used theoretical calculations by Rein and Sehgal [34] to predict the rate and kinematics of neutrino resonance production. Such models are tuned to reproduce neutrino single pion data, but remain poorly constrained, because of the limited availability and large uncertainties in existing experimental data. As an example, Figure 2.7 shows the experimental constraints on CC single π^0 production. Note that some of the data are conflicting and all of the data at low energy were collected from light targets.

By contrast, Figure 2.8 shows the only available experimental measurement of an absolute resonant NC π^0 cross section, which was collected on a propane-freon target and at only a single energy. This NC data point results from a recent reanalysis of Gargamelle bubble chamber data at 2.2 GeV [36]. Because the NC cross sections are

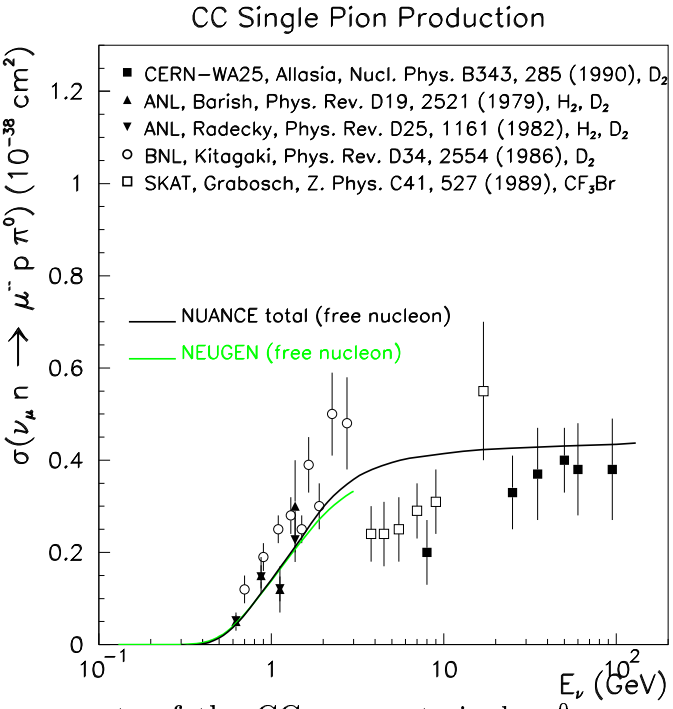

Figure 2.7: Measurements of the CC resonant single π^0 cross section, $\sigma(\nu_\mu\, n \rightarrow \mu^-\, p\, \pi^0)$. Also shown are the Rein and Sehgal-based predictions from two publicly available Monte Carlo generators [35].

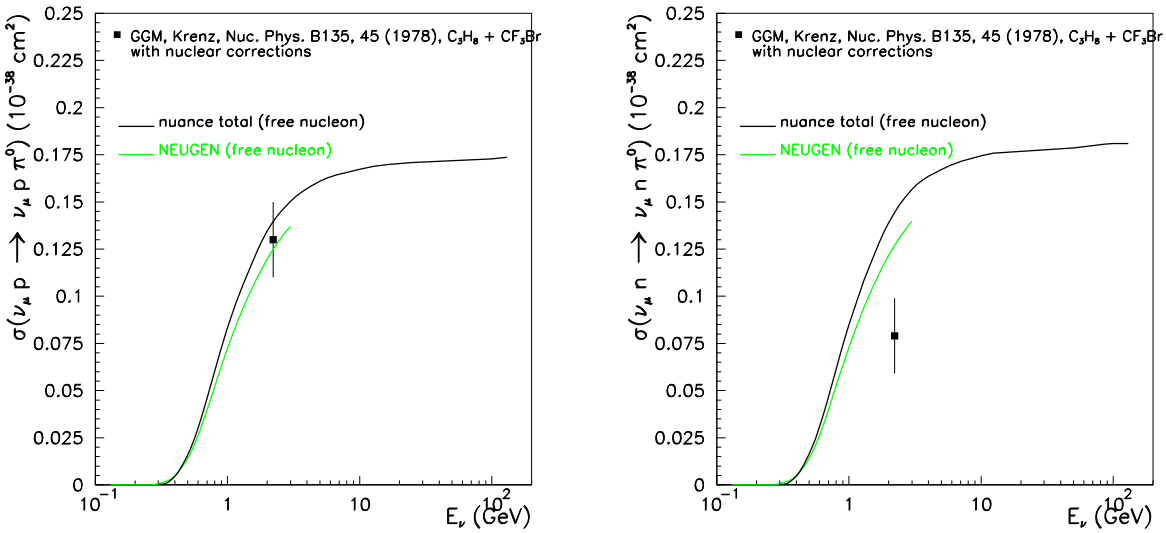

Figure 2.8: NC resonant single π^0 cross sections, $\sigma(\nu_\mu\, p \to \nu_\mu\, p\, \pi^0)$ (left) and $\sigma(\nu_\mu\, n \to \nu_\mu\, n\, \pi^0)$ (right). Also shown are the Monte Carlo predictions from [35].

less well known, in practice, experiments typically assign large $25-30\%$ uncertainties to NC resonant production processes.

At these low energies, the data are even more sparse for the other contributing production mechanism, coherent single pion production. In coherent interactions, neutrinos scatter off the entire nucleus rather than its individual constituents. Because of the negligible energy transfer to the target nucleus (A), such processes distinctly provide a single forward-scattered pion. Like in the resonant case, both NC and CC processes are possible:

$$\begin{aligned} \nu_\mu\, A &\to \nu_\mu A\, \pi^0 \\ \nu_\mu\, A &\to \mu^- A\, \pi^+ \end{aligned}$$

Almost all Monte Carlo simulations in current use base their predictions on Rein and Sehgal's original calculation [40] of coherent pion production cross sections and kinematics. While such predictions have been constrained by numerous experimental measurements at high energy [37], the lowest energy data available is at 2 GeV on an aluminum spark chamber target [38]. Figure 2.9 shows the low energy Aachen measurement compared to several model calculations.

More recent calculations [39] yield a factor of 2-20 less coherent pion production at these energies than the earlier Rein and Sehgal predictions [40]. Because of the

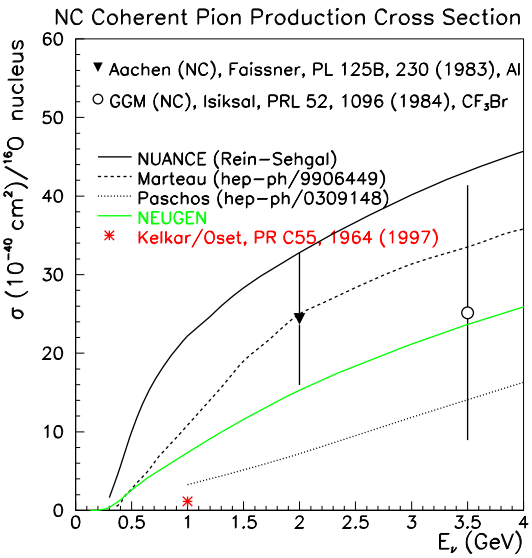

Figure 2.9: Experimental measurement of the NC coherent π^0 production cross section at low energy compared to current model predictions [39],[40].

lack of low energy experimental data and the existence of several conflicting theoretical predictions, oscillation experiments typically assign a 100% uncertainty to coherent processes. This large uncertainty is especially important because coherent production may comprise up to 20% of the overall NC π^0 rate. The ability to further constrain NC π^0 production at low energies would thus be of great use in achieving increased sensitivity to $\nu_\mu \rightarrow \nu_e$ oscillations, and in placing more stringent limits on the oscillation of standard neutrinos to sterile states.

With its ability to isolate π^0 interactions, this experiment would be the first to precisely measure NC π^0 (and CC π^0) production on carbon at these energies ($\langle E_\nu \rangle \sim$ 700 MeV), thus providing an important constraint to oscillation experiments such as MiniBooNE, as well as to other accelerator- and atmospheric-based ν_e appearance experiments employing heavy nuclear targets. Such efforts also complement slightly higher energy ($\langle E_\nu \rangle \sim 1.3$ GeV) scintillator-based analyses currently being planned with upgrades to the K2K near detector site [41].

Strange Particle Production

Proton decay modes containing a final state kaon, $p \rightarrow \nu K^+$, have large branching ratios in many SUSY GUT models. Because there is a non-zero probability that an

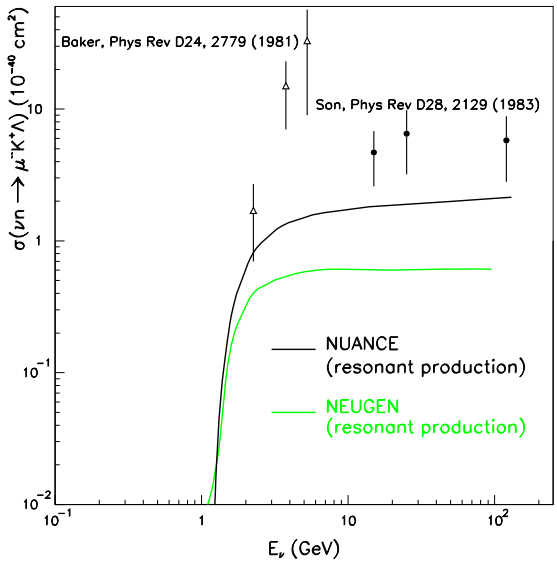

Figure 2.10: Experimental measurements of the $\nu_\mu n \to \mu^- K^+ \Lambda$ cross section. Also shown are the predictions from two publicly available Monte Carlo generators [35].

atmospheric neutrino interaction can mimic a proton decay signature,

$$\nu_\mu\, n \to \mu^-\, K^+\, \Lambda$$
$$\nu_\mu\, p \to \nu_\mu\, K^+\, \Lambda,$$

it is important to reliably estimate this background. Present uncertainties on this background process are as large as 100% [42] both because neutrino strange particle production rates have been measured in only a few experiments, and because theoretical models cannot suitably constrain them [43]. Figure 2.10 shows results from the only two experiments which have published cross sections on the dominant associated production channel, $\nu_\mu\, n \to \mu^-\, K^+\, \Lambda$. Both measurements were made on a deuterium target and were based on less than 30 events combined.

The ability to successfully isolate such interactions requires use of a fine-grained detector such as the one being proposed here. Measurement of this process in this case would be an important step toward constraining this production mechanism near threshold and on nuclear target (both of which are most relevant for proton decay searches).

The importance of low energy neutrino cross section measurements has been recognized in the wider neutrino community. The 2004 APS Multidisciplinary Study

on the Future of Neutrino Physics cites as a high priority the need to better measure neutrino cross sections in the MeV-to-GeV range [44].

With the measurements described here, this experiment would satisfy this need and thereby provide a major missing piece to the global neutrino program.

Chapter 3

The Neutrino Beam and Expected Event Rates

A new beamline built in the existing U-Line off of the Fast Extraction area at the AGS can provide the world's highest intensity neutrino beam in the $0.5 - 1.0$ *GeV neutrino energy range. The necessary statistics for this experiment can be accumulated with this beam within 4 months, running concurrently with the RHIC program, prior to RSVP.*

Neutrino physics has a long history and bright future at the AGS. Beginning with the discovery of the muon neutrino [45], and through searches for neutrino oscillations and neutrino scattering physics, a large body of published work on neutrino physics has been produced by experiments at Brookhaven. AGS upgrades over the last 10-15 years have allowed for significant increases in intensity in the machine, necessary for the existing program but also paving the way for near-future, parasitic, neutrino physics experiments such as described here. Continued improvements and upgrades to the AGS and its front end can make the machine into a high intensity proton driver capable of producing beams for very long baseline experiments in the farther future [46]. This experiment can help to initiate this new era of neutrino physics at Brookhaven.

A neutrino beam can be produced using the fast extracted beam (FEB) area in AGS U-Line, for the near-term neutrino physics measurements as described in this LOI. These physics measurements require proton delivery from the AGS for approximately 4 months, running parasitically with the RHIC program, and prior to

the RSVP program. The intensity needs for this experiment are well within what is already planned for the RSVP program the following year. This chapter describes the details of this proton delivery, the target hall, horn system, decay region, and the subsequent neutrino flux and detected event rates.

3.1 The AGS Neutrino Beam

Conventional high intensity neutrino beams are produced from pion and kaon beams decaying in flight. High intensity proton beams incident on fixed targets produce these meson beams, directed by a focusing system, toward a detector. In order to produce a high intensity, relatively low energy neutrino beam, a high intensity proton beam is necessary. The project described here requires a total of 1.5×10^{20} protons on target (POT). The nominal beam momentum is 8 GeV/c, but this can be adjusted slightly depending on other BNL operational considerations.

3.1.1 Protons from the AGS

The AGS can presently operate at 30×10^{12} protons (or 30 TP) per second. For this project, the AGS will nominally deliver this, in beam spills of 30 TP at 1 Hz to the FEB line. These spills are 3 microseconds long and composed of 2 or 4 bunches, depending on the AGS Booster's operation. In the case of 2 bunches the bunch length is less than about 50 nanoseconds, and each bunch has 15 Tp (1.5×10^{13} protons) [47].

Radiation levels at extraction in the FEB area at these intensities will need to be evaluated. Remediation is not expected to be a large cost item, and if necessary, the hourly beam rate for the project could be reduced. In the latter case the number of weeks of beam time must be increased to assure the total POT, and hence experimental sensitivity, remains the same.

Recent AGS demands for RHIC indicate an idle time that could accommodate 80 beam hours per week for this project. Thus, the project requires 18 weeks of calendar beam time. (1.5×10^{20} POT/30×10^{12} POT/sec = 5×10^{6} seconds = 1389 hours = 17.4 weeks at 80 hours per week.)

3.1.2 The Neutrino Beamline

Protons, incident on a berylium target, produce pions and kaons that then decay primarily into muons and muon neutrinos. The pions and kaons are focussed toward the neutrino detector, before they decay, by a magnetic focusing system (or horn) surrounding the target. The design for this target plus horn system is the same as that used in the MiniBooNE experiment [48].

This neutrino beam can be sited in the existing U-line which splits off from the X and Y lines servicing RHIC, downstream of the FEB extraction area. There is an existing neutrino blockhouse just downstream of where this line splits off. The tunnel continues for 85 m beyond this followed by a 12 m steel absorber. There are no plans to use this beamline in the near future.

As described, the existing neutrino blockhouse sits 85 meters from the end of the decay channel. The optimal decay length for maximizing neutrino flux at the detector location at these energies is 25 m. To reduce the decay length from 85 m to the 25 m requires a new neutrino block house will have to be excavated in the existing decay region. The work required for this is likely as much as updating the existing blockhouse. Installing a new blockhouse requires additional shielding around the berm as well as a place to house the horn power supplies. It is not clear whether or not more space is required in the beamline to house a horn. However, there is an existing labyrinth and a slightly larger space than the beam tunnel already at this location which may accomodate the horn focussing system.

Radiation levels in and around a neutrino horn require shielding and ground water protection. Following preliminary discussions with the Radiation Safety Group at the AGS, the updates required to the existing shielding on the U-Line horn include installation of a neutrino liner, and an additional, approximately 8 ft. of overburden on top of the existing 10 ft. of overburden.

At the end of the U-Line, there is an existing 12 m, steel beam absorber stacked normal to the beam. This beam absorber, larger than the one MiniBooNE uses, is more than adequate to absorb unwanted meson decay products in this neutrino beam.

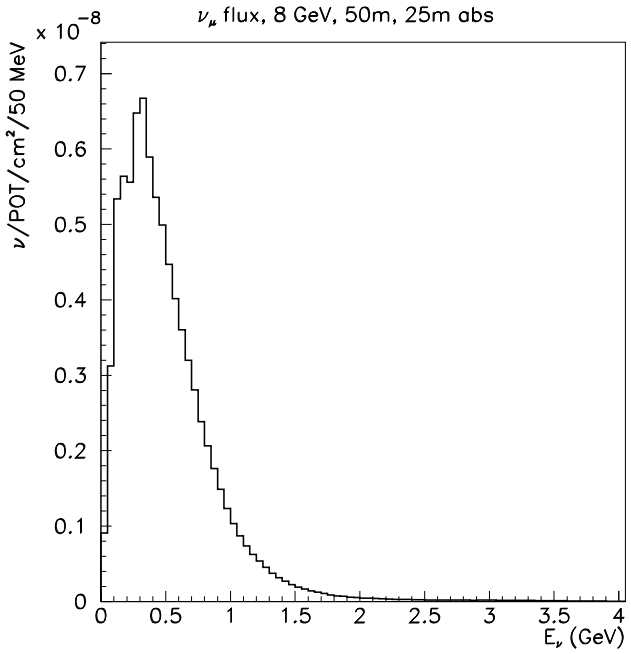

Figure 3.1: *Expected ν_μ flux at a 50 m detector site assuming a 25 m decay length and 8 GeV primary proton beam.*

3.1.3 The Neutrino Flux

Figure 3.1 displays the expected muon neutrino flux for this experiment, at a 50 m distance, assuming an 8 GeV incoming proton beam, and a 25 m decay length. This flux was simulated using the same tools currently being employed by the MiniBooNE collaboration [50] and assumes the same proton target (beryllium) and horn geometry as the MiniBooNE target design.

In this configuration, 84.3×10^{-9} muon neutrinos per POT per cm^2 are anticipated with a mean energy of $\sim$ 500 MeV. Figure 3.2 shows the individual contributions to the total predicted neutrino flux. 92.2% of the beam is muon neutrino. Contaminations from $\overline{\nu_\mu}$'s and ν_e's are predicted to be 8% and 0.5% of the total ν_μ flux, respectively. However, once the "wrong–sign" $\overline{\nu_\mu}$ background events are weighted by their appropriate cross section, they will comprise less than 2% of the total events in the detector.

The ability to accurately measure neutrino cross sections will require precise knowledge of the incoming neutrino flux. The neutrino flux produced from such 8 GeV proton-beryllium interactions will be much better known than the fluxes reported in the previous generation of bubble-chamber-based low energy neutrino cross

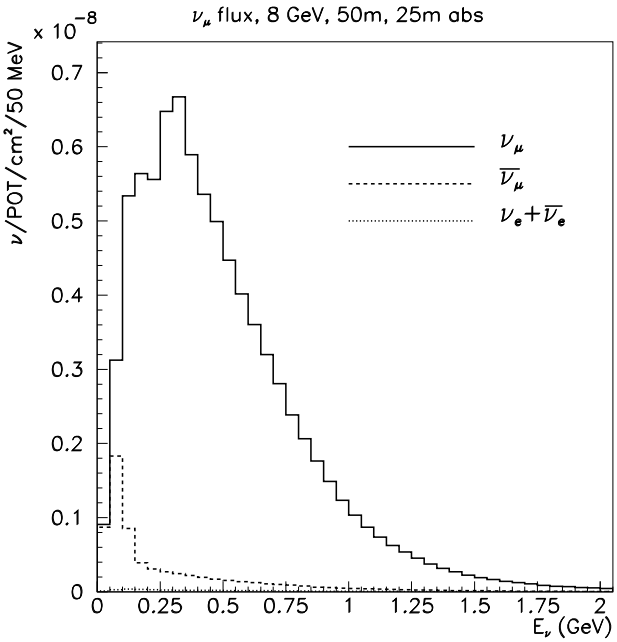

Figure 3.2: Predicted flux contributions at a 50 m detector site assuming a 25 m decay length. Muon neutrinos comprise more than 90% of the expected neutrino flux.

section measurements. This improved knowledge comes from two sources: data from the Brookhaven E910 experiment [51] and from the CERN HARP experiment [52]. Analysis that is already underway of E910 proton-beryllium data taken at 6, 12, and 18 GeV beam energies will be instrumental in verifying the extrapolation of pion production parameterizations to an 8 GeV beam energy. More importantly, HARP data taken at 8 GeV on beryllium target slugs of varying thicknesses will provide an even tighter constraint on the flux. The high statistics HARP data will provide a statistical precision of $\sim 2\%$ [53] on π^+ production, which is the main source of muon neutrinos for this experiment. Therefore, with these additional inputs, the overall muon neutrino flux should be known to roughly 5% [50].

3.2 Neutrino Event Rates

The number of neutrino events expected in the proposed scintillator-based detector is calculated using cross section predictions from the NUANCE Monte Carlo [54]. NUANCE is open-source code originally developed for simulating atmospheric neutrino interactions in the IMB detector. NUANCE has since been further developed and is

now used by the K2K, Super-K, SNO, MiniBooNE, and MINERvA collaborations. The neutrino interaction cross sections in NUANCE have been extensively checked against published neutrino data and other available Monte Carlo event generators. In addition, the full NUANCE simulation has been recently shown to provide a good description of neutrino events in both the MiniBooNE detector and K2K near detector ensemble.

For this specific use, NUANCE was modified to include the detector composition and geometry, as well as the incident neutrino flux at the 50 m detector site (Section 3.1.3). Using the input neutrino flux distribution, NUANCE predicts event rates, kinematics, and final state particle topologies that can subsequently feed hit-level GEANT detector simulations, or, as in this case, simply estimate the type and number of neutrino interactions expected at the detector.

Table 3.1 lists the NUANCE-predicted event populations at the 50 m BNL detector site assuming a 25 m decay length. The table provides the expected ν_μ rates per ton detector for 1×10^{20} POT as well as the expected backgrounds from the $\overline{\nu_\mu}$ and ν_e content in the beam. Note that the beam has very low non-ν_μ backgrounds. Roughly 1.6% (0.5%) of the total neutrino events result from $\overline{\nu_\mu}$ (ν_e) interactions in the detector. The dominant contributions to the total event rate result from elastic and resonant processes: 47% of the ν_μ events are CC quasi-elastic ($\nu_\mu\, n \to \mu^-\, p$), 20% are NC elastic ($\nu_\mu\, N \to \nu_\mu\, N$; $N = n, p$), and 16% resonant single pion production ($\nu_\mu\, N \to \mu^-\, (\nu_\mu)\, N\, \pi$) interactions.

A total of approximately 300,000 muon neutrino interactions can be expected at the proposed detector site assuming 1.5×10^{20} protons on target. This raw estimate assumes a 9 ton fiducial detector and 100% detection/reconstruction efficiency.

ν interaction type	ν_μ 10^{20} POT 1 ton	$\overline{\nu_\mu}$ 10^{20} POT 1 ton	$\nu_e + \overline{\nu_e}$ 10^{20} POT 1 ton
CC QE, $\nu_\mu n \to \mu^- p$	11,395	184	56
NC EL, $\nu_\mu N \to \nu_\mu N$	4,993	86	22
CC π^+, $\nu_\mu p \to \mu^- p \pi^+$	3,293	24	24
CC π^0, $\nu_\mu n \to \mu^- p \pi^0$	725	11	6
CC π^+, $\nu_\mu n \to \mu^- n \pi^+$	646	10	6
NC π^0, $\nu_\mu p \to \nu_\mu p \pi^0$	606	10	5
NC π^+, $\nu_\mu p \to \nu_\mu n \pi^+$	370	6	3
NC π^0, $\nu_\mu n \to \nu_\mu n \pi^0$	454	8	3
NC π^-, $\nu_\mu n \to \nu_\mu p \pi^-$	290	5	2
CC DIS, $\nu_\mu N \to \mu^- X$	176	0	1
NC DIS, $\nu_\mu N \to \nu_\mu X$	64	0	0
CC coh π^+, $\nu_\mu A \to \mu^- A \pi^+$	539	22	3
NC coh π^0, $\nu_\mu A \to \nu_\mu A \pi^0$	349	14	2
other	464	14	1
total	24,364	394	134

Table 3.1: *Number of events expected at 50 m with a 25 m decay length for* 1×10^{20} *POT per ton detector. These predictions do not include final state effects and assume* 100% *detection/reconstruction efficiency.*

Chapter 4

The Detector

A novel detection technique, described here, accurately measures short-track neutral current events at all angles, particularly high angle, low Q^2 events most important for the Δs analysis. This fine-grained detector can also well measure single pion channels and quasi-elastic events.

The physics goals for this experiment require the ability to identify and track charged particles in $0.1 - 2.0$ GeV neutrino interactions. These reactions include neutral-current (NC) elastic scattering ($\nu_\mu p \rightarrow \nu_\mu p$, $\nu_\mu n \rightarrow \nu_\mu n$), charged-current (CC) quasi-elastic scattering ($\nu_\mu n \rightarrow \mu^- p$), as well as neutral- and charged-current production of pions ($\nu_\mu p \rightarrow \nu_\mu \pi X$, $\nu_\mu n \rightarrow \mu^- \pi X$). It is necessary to measure both the charged hadrons and charged leptons in these reactions. The detector must also provide a large target volume in order to achieve the event rates needed to gather sufficiently large event samples.

4.1 Detector Overview

The detector will consist of a 13 ton (9 ton fiducial) liquid-scintillator, wavelength-shifting (WLS) fiber Vertex Detector with a downstream Muon Rangestack. The Vertex Detector will track particles as they emerge from the neutrino interaction vertex as well as measure the energy of the final state baryons. The Muon Rangestack, consisting of alternating planes of scintillator and iron, will range out and, therefore,

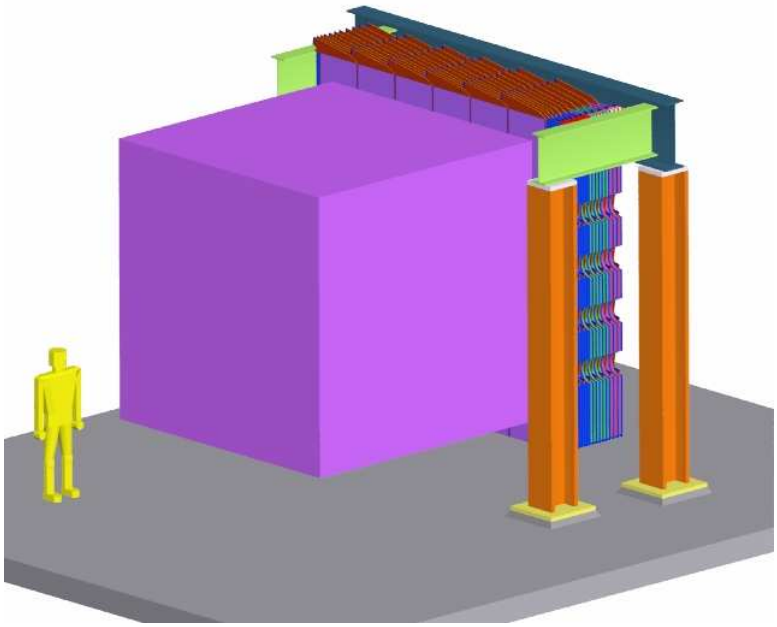

Figure 4.1: A schematic drawing of the detector. The cubic volume is the $(3.5\text{m})^3$ Vertex Detector. The $(2.4\text{m})^3$ signal region is surrounded by a veto, filled with liquid scintillator. The volume downstream consisting of multiple layers is the Muon Rangestack.

measure the energy of the muons produced in CC reactions. This detector arrangement is shown in Figure 4.1. The cost estimate for this detector, with contingency, is \$2.8M.

An option to add an approximately 20 ton liquid Argon time projection chamber just upstream of the Vertex Detector is currently under study. This detector is not required to achieve the physics goals quoted in this Letter, but could possibly enhance the program in the future.

4.2 The Vertex Detector

As the name suggests, the Vertex Detector provides the neutrino target and is fully instrumented. This allows us to precisely track the final-state particles in order to accurately determine the vertex location and event kinematics. The detector also measures energy loss ("dE/dx") to help in separating proton and muon tracks. The

physics goals require a combination of high-efficiency tracking and good energy reconstruction for protons down to a kinetic energy of 100 MeV. This necessitates a detector that has both fine segmentation and good calorimetry.

The Vertex Detector uses a technique called "scibath" which consists of WLS fibers immersed in a volume of liquid scintillator. The central liquid scintillator volume has dimensions of $2.4 \times 2.4 \times 2.4$ m^3. Light generated by ionizing particles traversing the scintillator is picked up by 1.5 mm diameter WLS fibers, submerged throughout the sensitive volume. There is no optical separation between the fibers. The fibers are mounted on a support frame, and are connected on one end to multi-anode photomultipliers, mounted to the outside of that frame. The fiber frame, photomultipliers, and associated electronics form a unit; this unit is immersed in the liquid scintillator, which is contained in a cubic tank, 3.5 m on a side. The volume between the fiber structure and the tank wall is instrumented with 2 layers of fibers with a spacing to be determined in order to detect and reconstruct charged particles entering and exiting from the tracking volume ("veto region"). The photomultiplier signals are processed *in situ* and transmitted on a data bus (Ethernet or similar) to the outside of the tank, thus minimizing the number of cables that penetrate the tank wall. A schematic drawing of the tracking detector is shown in Fig. 4.2. Cables penetrate the tank wall above the oil level to simplify leak-prevention.

Particle tracks can be reconstructed because the relative amount of light detected at the end of a fiber from a given source inside the detector is a known, continuous function of the distance between the source and the fiber.

The arrangement of the WLS fibers is shown schematically in Fig. 4.3. There are three sets of fibers, running parallel to the axes of a Cartesian coordinate system. Except for a rotation in space and an offset, the three fiber sets are identical, consisting of fibers that intercept the wall at the vertices of a quadrate grid. The distance between grid points is 30 mm. Thus, the closest distance between any two fibers in the full assembly is 15 mm. The resulting arrangement is invariant with respect to a rotation by 90° about any major axis. For the given dimensions, there are a total of $80 \times 80 \times 3 = 19200$ fibers.

This unique arrangement of fibers in the liquid scintillator volume offers several advantages over other detectors used in similar applications. There is no optical separation between the WLS fibers as is commonly employed in solid scintillator neutrino detectors [55]. This allows for greater sampling of the light produced by charged par-

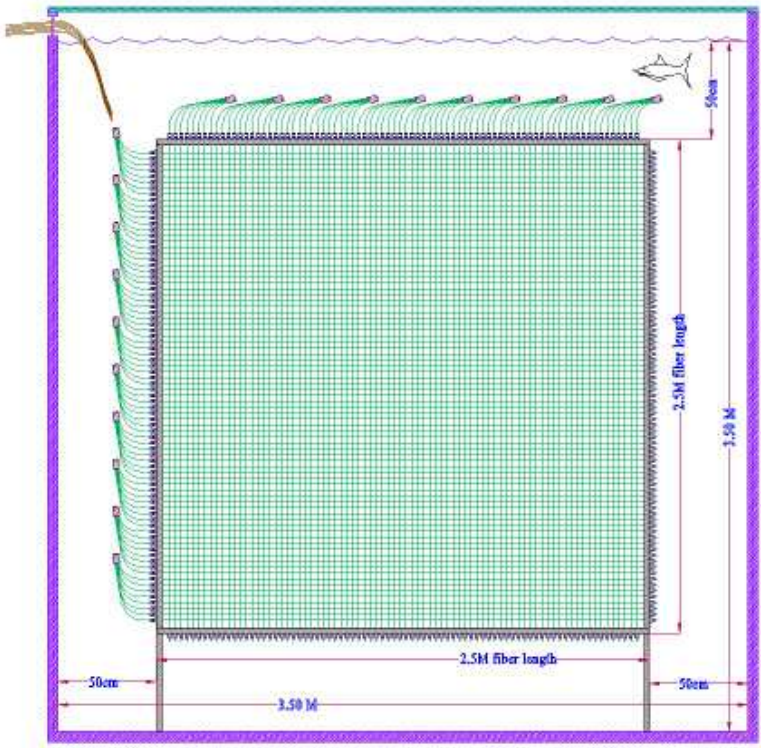

Figure 4.2: A schematic projection view of the Vertex Detector.

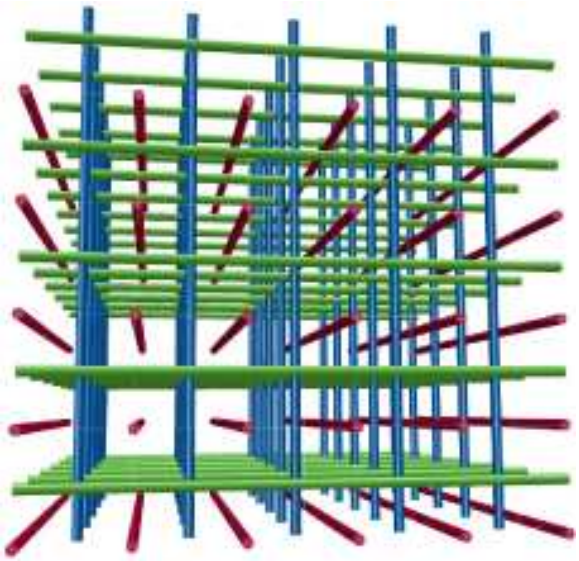

Figure 4.3: The geometrical arrangement of WLS fibers inside the Vertex Detector. The arrangement consists of three orthogonal sets of parallel fibers. The geometry is symmetric with respect to a rotation by 90° about any of the three major axes.

ticle tracks which results in better tracking precision, especially for the short proton tracks that are of major interest in these physics measurements. A 100 MeV proton travels only about 10 cm in liquid scintillator. In a solid scintillator bar detector, these tracks may only leave light in a few fibers which does not allow for good reconstruction of the track. However, in the "scibath" detector, these proton tracks will create light that is intercepted by several dozen fibers. This greater sampling allows for superior reconstruction, even for short tracks.

The arrangement of fibers in this detector with a grid parallel to each of the three major axes allows for three simultaneous track projections to be reconstructed. This is not possible in solid scintillator detectors or liquid scintillator detectors with optical separation between fibers. This technique results in better efficiency for tracks at 90° to the beam direction. These tracks frequently produce light in a small number of fibers as they are parallel to one of the fiber directions. The scibath method avoids this problem as the tracks are at large angles with at least two of the three fiber directions.

4.2.1 Prototype Tests

The scibath method has been tested using a ($16 \times 16 \times 30$ cm^3) prototype in the 200 MeV proton beam at the Indiana University Cyclotron Facility. The prototype contained a 6×5 grid of 1.5 mm diameter, WLS fibers (Bicron BCF-91A-MC, [56]) on 20 mm spacing and was filled with liquid scintillator (Bicron BCS517H [56]). The fibers were routed on one end to two 16-anode photomultiplier tubes (Hamamatsu H8711 [57].)

Results from these tests yielded 6 mm position resolution and 6° angular resolution with 17 photoelectrons detected for a proton track passing within several mm of a fiber (see Figure 4.4) . These numbers will vary in a full-sized detector depending on the type and energy of particle. These results for 200 MeV protons were used to tune the Monte Carlo simulation program used to predict physics results.

Additional tests have been conducted using different WLS fibers in a scintillator with a different mixture of wavelength shifter. These tests were motivated by the desire to tune the attenuation length of the liquid scintillator and therefore the energy sharing between fibers. Preliminary results from these tests show that the light is better localized in the detector allowing multiple tracks to be more easily separated. In

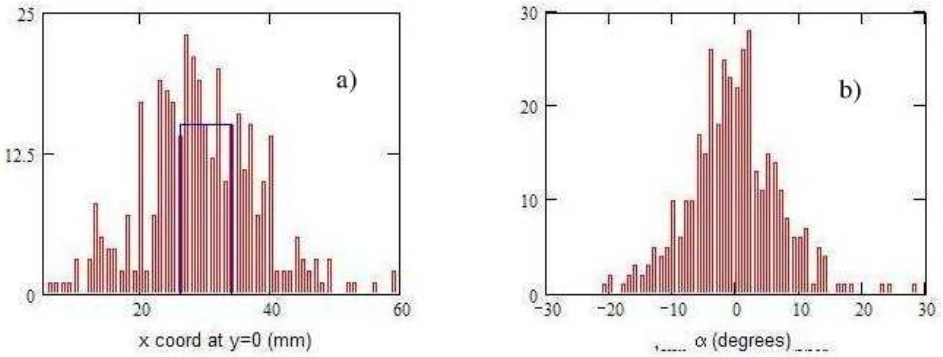

Figure 4.4: Reconstructed track position (a) and angle (b) for a sample of 200 MeV protons in the scibath prototype detector. This data yielded a 6mm position resolution and 6° angular resolution. The rectangle overlay in (a) shows the extent of the trigger scintillators.

addition, several different promising scintillator/fiber combinations have been shown to produce more light.

4.3 The Muon Rangestack

The Muon Rangestack is located just downstream of the Vertex Detector. This subdetector, in conjunction with the Vertex Detector, is designed to range out muons with energies up to 1.5 GeV, allowing for a measurement of the muon energy. These characteristics are needed to enable the reconstruction of CC ν_μ events. Because the muons from high energy CC ν_μ events tend to be produced at forward angles, the Rangestack need only provide adequate acceptance for coverage in the forward direction.

The iron absorber planes and tracking granularity in the Rangestack are designed to meet these requirements. The stack is comprised of 4×4 m^2 alternating planes of scintillator strips and iron absorber with an overall depth of 0.85 m (0.98 m including support structure) in the beam direction, and a weight of 100 tons. Of the 0.85 m thickness, 0.24 m is scintillator and 0.61 m is iron. This design meets the physics requirements while minimizing cost and space demands.

The Rangestack may be seen in Figure 4.5 situated behind the Vertex Detector. The structural steel shown supporting the stack is a conceptual design. The PMT

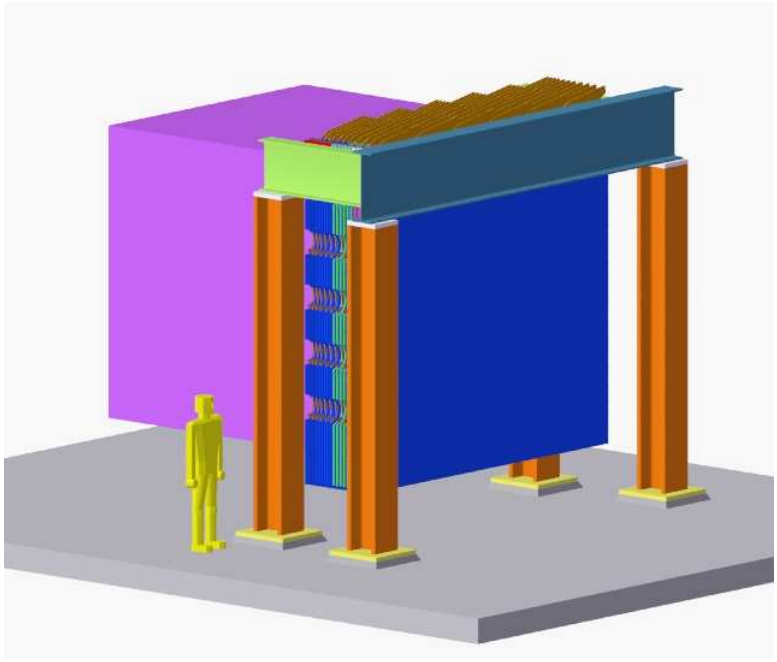

Figure 4.5: An schematic drawing of the detector from the backside showing the multiple layers of steel and scintillator that comprise the Muon Rangestack.

enclosures or clear fiber bundles surrounding the Rangestack are not shown here.

4.4 Signal Readout: Phototubes and Electronics

A common design for signal readout will be used for the Vertex Detector and the Muon Rangestack. Requirements for the readout system include independent amplitude and timing measurements for each channel. The amplitude information is used in the track reconstruction and for dE/dx measurement for the particle tracks; timing information is used to assemble the hits (rejecting spurious noise hits and background tracks), to correlate with the beam spills, and in the analysis of secondary events such as muon decay and nuclear decay in the active volume following the capture of a neutron produced in the primary event. In the Vertex Detector, the full scale signal range will extend to > 50 PE, with an amplitude resolution of < 0.1 PE. The timing resolution is not crucial, but needs to be $\sim$10 ns to reduce spurious hits and background tracks.

The readout must be sensitive both to the primary interaction events (which are in time with the beam spill) and to secondary events as described above. It is also

useful that it be sensitive to cosmic ray muon tracks, for calibration purposes. For these reasons, the front end electronics must be self-triggering and have a relatively low deadtime after being hit. Deadtime of the proposed system is about $1 - 5$ μs, depending on signal amplitude. The deadtime applies independently to each channel – this is a matter of recovery of the front end electronics only, since there is zero deadtime associated with the data readout. A external global trigger will also be implemented, which can be used to force an event readout and/or a charge pulser event, for diagnostic purposes.

The readout system designed to meet these requirements combines 64-channel multianode photomultiplier tubes (MAPMTs) and custom readout electronics in a 128-channel "readout module." This includes two MAPMTs (Hamamatsu R7600-00-M64 or equivalent), front end electronics, HV bias circuits, charge-injection test pulsers, and data acquisition and control communications. This design is quite similar to that recently employed for the STAR Endcap Electromagnetic Calorimeter shower-maximum detector [58]. The module is a sealed, conductively cooled unit suitable for submerged operation inside the oil tank (for the Vertex Detector application). In the Muon Rangestack the readout modules will be mounted on the sides of the detector. The Vertex Detector requires 150 modules for readout of the active volume and six modules for the veto shield. The Muon Rangestack readout requires an additional 17 modules.

4.5 A Possible Future Upgrade: Liquid Argon Time Projection Chamber

A Liquid Argon TPC is not necessary to achieve the physics goals presented in this Letter, but, if installed at some time in the future, has the potential to substantially enhance the experiment. Liquid Argon TPC's combine bubble chamber quality resolution with active readout giving them great promise for precision neutrino scattering measurements. However, the technology has taken some thirty years to reach maturity predominately because of difficulties handling impurities in Liquid Argon. While the ICARUS collaboration in Europe has shown results from prototype Liquid Argon TPCs as large as 600 tons [59], the technology has not yet been widely used outside of this collaboration.

The feasibility of this technology for the set of measurements set forth here is currently under active study. If demonstrated to be feasible and worthwhile through an on-going R&D program and Monte Carlo studies, a small ($\sim$20 ton) Liquid Argon TPC could be installed upstream of the existing Vertex Detector to enhance these precision neutrino scattering measurements. The rest of this section provides a brief description of how these detectors work and some of the issues regarding construction and operation of a $\sim$20 ton Liquid Argon TPC detector.

4.5.1 Detection Technique and Detector Construction

Charged particles are detected in Liquid Argon TPCs via ionization electrons produced along the path of the passing particle. These ionization electrons drift over several meters to the edge of the chamber where they are readout via wire chamber planes. In order for the drifting electrons to travel on the order of a meter in Argon, without being captured, the impurity levels must be less than 0.1 ppb in the Argon. This purity level is achieved by passing the Argon through oxisorb/hydrosorb standard filters. The entire detector must be housed within a large cryostat and have an active Argon purification system.

Ionization electrons are read out on three wire chamber planes with wires at 3 mm pitch, rotated by 60° with respect to each other. The first two planes read the charge induced by the passing electrons and the third collects the charge. In a neutrino beam, the time of an event can typically be determined to $\sim 1\ \mu s$ from beam timing. This corresponds to a negligible 1 mm drift in the Liquid Argon. Therefore, beam timing can be used to determine the initial time of an event. This information combined with the drift time, and the wire chamber readout, allows for a 3D track reconstruction. Figure 4.6 shows a stopped cosmic ray muon track and the decay electron as read out from the 600 ton ICARUS Liquid Argon TPC [59].

Scintillation light is also produced in copious amounts in Liquid Argon. ICARUS has detected scintillation light levels in its 600 ton prototype via Hamamatsu 8 inch Photomultiplier tubes [59]. Scintillation light may provide an additional handle for particle identification.

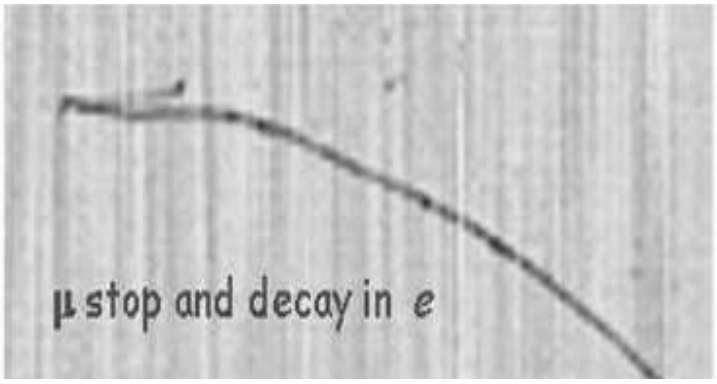

Figure 4.6: A stopped cosmic ray muon and its decay electron, in the ICARUS T600 prototype [59].

4.5.2 R&D program

In order to independently understand and verify the feasibility of this technology, we are building a small, $\sim$ 50 liter Liquid Argon TPC prototype. The goal of this work is to demonstrate the technology within our group and to allow us to identify any unforeseen problems. In conjunction with building a prototype, we are studying the specifics of neutrino interactions in this kind of detector using detailed Monte Carlo simulations. Throughout this process, we have been in contact with members of the ICARUS collaboration who have been extremely helpful and supportive of our initiative [60].

4.6 Experimental Area at Brookhaven

The detector should be located as near to the neutrino source as possible to maximize event rate, but far enough away so as to avoid detecting unwanted particles produced in the beam absorber at the end of the decay channel. These requirements would site the detector 25m from the beam absorber, or 50m from the production target [49] as assumed in Chapter 3.

There is presently open space 25m downstream of the end of the U Line, so construction of this experiment includes the construction of a building to house the detector.

While the detector hall should be large enough to accommodate the detectors

and their associated electronics, it can remain a relatively simple enclosure. Should the building need to additionally house cryogenics necessary for a Liquid Argon TPC detector, it will need to be modified.

Chapter 5

Physics Sensitivity

Physics events are simulated using a full GEANT3 Monte Carlo. Reconstruction of these events demonstrates that the physics goals of this experiment can be realized.

5.1 Introduction to Interactions in the Detector

The event rates expected in the Vertex Detector are listed in Table 3.1. The most important and most prevalent events occurring in the detector are listed in Table 5.1, along with a description of how they are observed in the detector.

event name	reaction	# tracks	description
CCQE	$\nu n \to \mu^- p$	2	μ,p: two-body kinematics
NCp	$\nu p \to \nu p$	1	p: two-body kinematics
NCn	$\nu n \to \nu n$	0	n: extraneous visible tracks from νp scattering
CCπ	$\nu n \to \mu^- X \pi^{\pm,0}$	$>\approx 2$	Not two-body kinematics
NCπ	$\nu p, n \to p, n X \pi^{\pm,0}$	$>\approx 1$	Not two-body kinematics

Table 5.1: Summary and description of event types in the detector. "# tracks" means typical number of charged particle tracks of significant energy.

Examples of typical simulated events are shown in Figures 5.1-5.3. In these figures, charged hadrons are shown as solid lines, muons as wide dashed lines, neutrinos

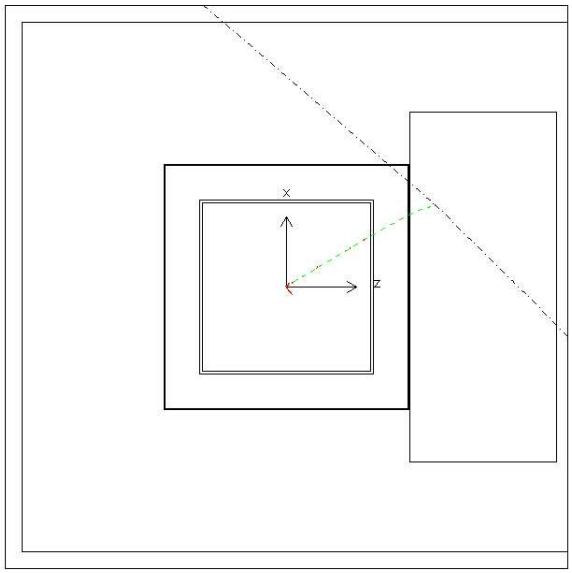

Figure 5.1: A typical $\nu n \to \mu^- p$ reaction in the detector. The event vertex is at the origin of the indicated coordinate system. In this example, the μ^- leaves the Vertex Detector, stops in the range stack, and decays. The two neutrinos (dot-dashed lines) from the muon decay are seen exiting the apparatus. The short recoil proton track is visible as a short stub at the origin.

and neutrons as dot-dashed lines, and photons as dotted lines. The detector is shown from the side.

The individual particles within a particular event will be identified via their track length, energy loss density, "dE/dx", and their decay pattern:

- $\mu^\pm$: Long tracks with low dE/dx. High-energy $\mu^\pm$ will exit the Vertex Detector, enter the veto, and perhaps the range stack. For $\mu^\pm$ that stop in an active area, the decay (Michel) electron will be observed.
- p: Short tracks with high dE/dx. A 100 MeV proton travels approximately 10 cm in liquid scintillator.
- n: Extraneous tracks from νp scattering. Occasionally transfer enough energy in one collision so as to be misidentified as a p track. Will thermalize and capture in the detector yielding a delayed 2.2 MeV γ.
- $\pi^\pm$: Longish tracks that look like $\mu^\pm$. For $\pi^\pm$ that decay in the active area of the detector, the subsequent $\mu^\pm$ and $e^\pm$ can be observed.

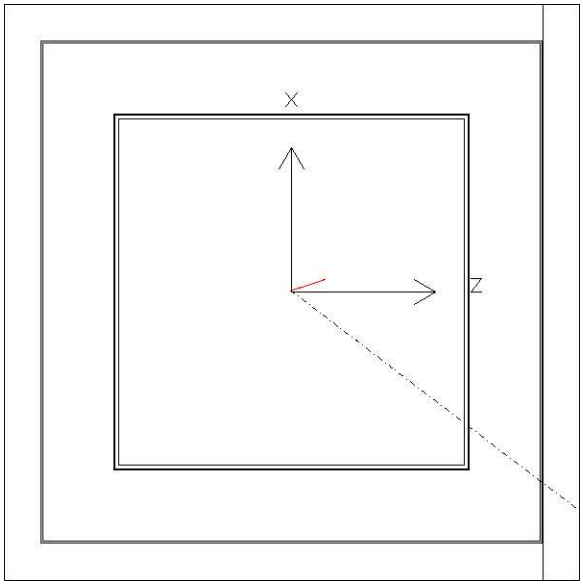

Figure 5.2: A typical $\nu p \rightarrow \nu p$ reaction expected in the detector, generated at the origin. The short proton track (solid line) can be seen, as can the final state neutrino (dot-dashed line) which exits the apparatus. In this view, only the Vertex Detector is shown.

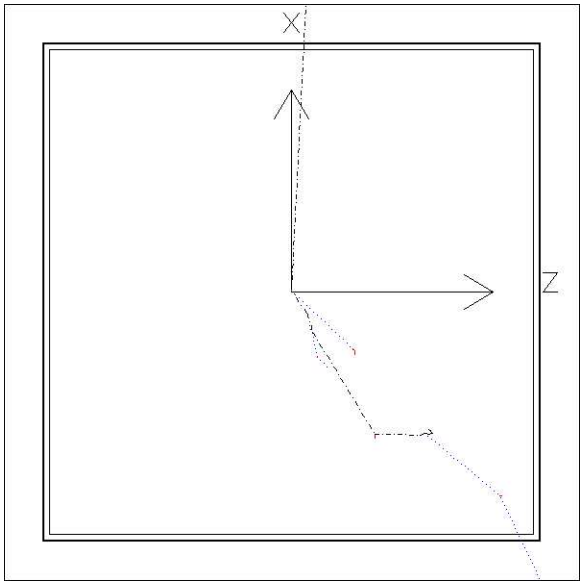

Figure 5.3: A typical $\nu n \rightarrow \nu n$ reaction expected in the detector. Several interactions of the final state neutron can be seen. The final state neutrino (dot-dashed line) exits the apparatus. In this view, only the Vertex Detector is shown.

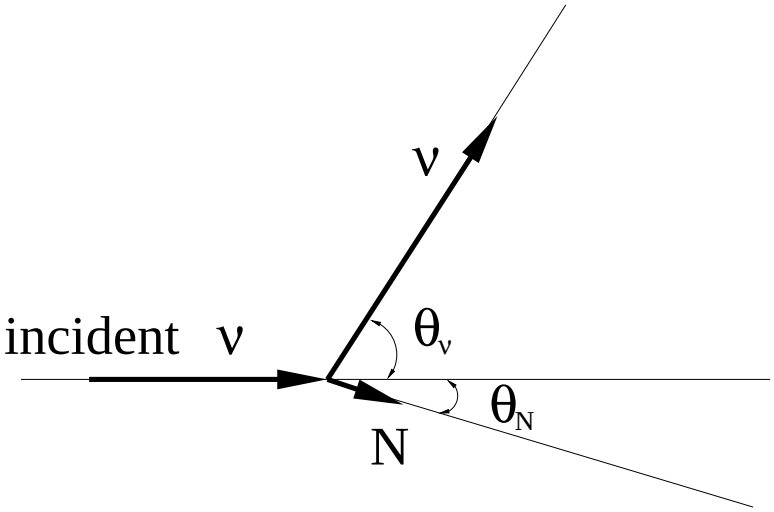

Figure 5.4: Illustration of the scattering angles for the NC elastic ($\nu p \to \nu N$) reaction. The CCQE ($\nu n \to \mu^- p$) reaction is similar, with the μ^- in place of the ν.

- π^0: 2 hit clusters from the π^0-decay γ showers.
- $e^{\pm}$: 1 "fat" track from the $e^{\pm}$ shower.

Event Kinematics

The two-body kinematics of NC elastic ($\nu N \to \nu N$) and CCQE ($\nu n \to \mu^- p$) interactions may be better understood by examining the scattering angle definitions in Figure 5.4 and the kinematic ellipses in Figure 5.5.

Due to the energy of the incident neutrino and the low mass of the muon compared to the hadron mass, the kinematics of the NCp and CCQE events are almost identical above $E_\nu \approx 300$ MeV. This simplifies the analysis and interpretation of the NC and CCQE event reconstruction. As can be seen in Figure 5.5, the final-state lepton may have any angle; the outgoing proton has a maximum lab angle of 90°. The correlations can also be seen in this figure. An event with a lower-energy high-angle lepton is paired with a low-angle high-energy proton (as in Fig. 5.4). And, a low-angle high-energy lepton is accompanied by a high-angle low-energy proton.

Plotting energy vs. angle (Fig. 5.6) reveals strong correlations between the two variables in such two-body reactions. The events of most interest for the Δs analysis are low Q^2 events, where the proton has a low energy and a high angle. The lepton

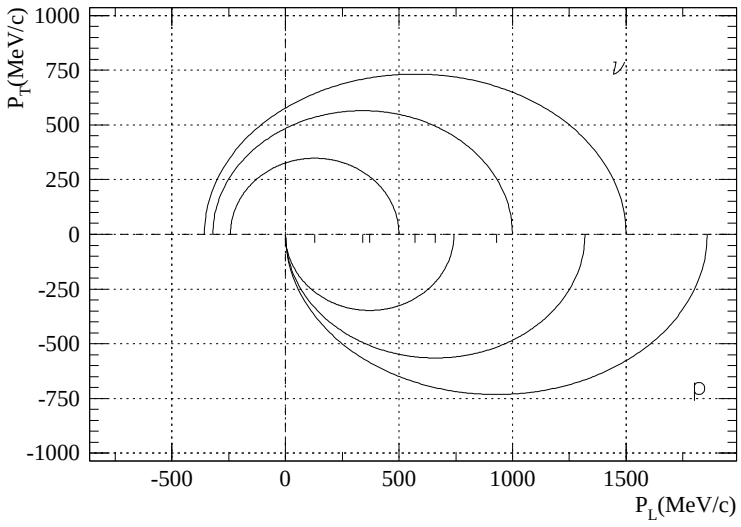

Figure 5.5: Kinematic ellipses for the NC elastic ($\nu p \rightarrow \nu p$) reaction. These are also valid for the CCQE ($\nu n \rightarrow \mu^- p$) reaction. The ellipses of increasing size indicate the lab momentum for the event at E_ν =500, 1000, 1500 MeV. The longitudinal component (parallel to the beam) of the particle momentum is plotted on the x-axis and the transverse component on the y-axis. In a particular event, the particle momentum vector is constrained to lie on the appropriate ellipse and in such a way to conserve momentum.

in these events will be in the forward direction at high energy. The events of most interest for the oscillation analysis are ν_μ CC interactions with outgoing muons whose kinetic energy lies in the 0.1 to 1.5 GeV range. Many of these lower energy muons range out in the Vertex Detector and veto; the most energetic ones, at small angles, enter and range out in the Muon Rangestack.

The effects of the Fermi momentum of nucleons can be seen in Fig. 5.6, which compares the final-state protons produced in CCQE scattering from nucleons bound in carbon (Fig. 5.6b) to those from free nucleon scattering (Fig. 5.6c). Fermi momentum widens the angular distribution of the outgoing proton and suppresses the number of nucleons at low momentum ("Pauli blocking"). The effect of this additional Fermi energy ($\approx$ 25 MeV) on the energy of the outgoing proton is small and will have minimal impact on measuring the Q^2 of the reaction (via $Q^2 = 2m_pT_p$ where m_p and T_p are the mass and kinetic energy of the proton respectively).

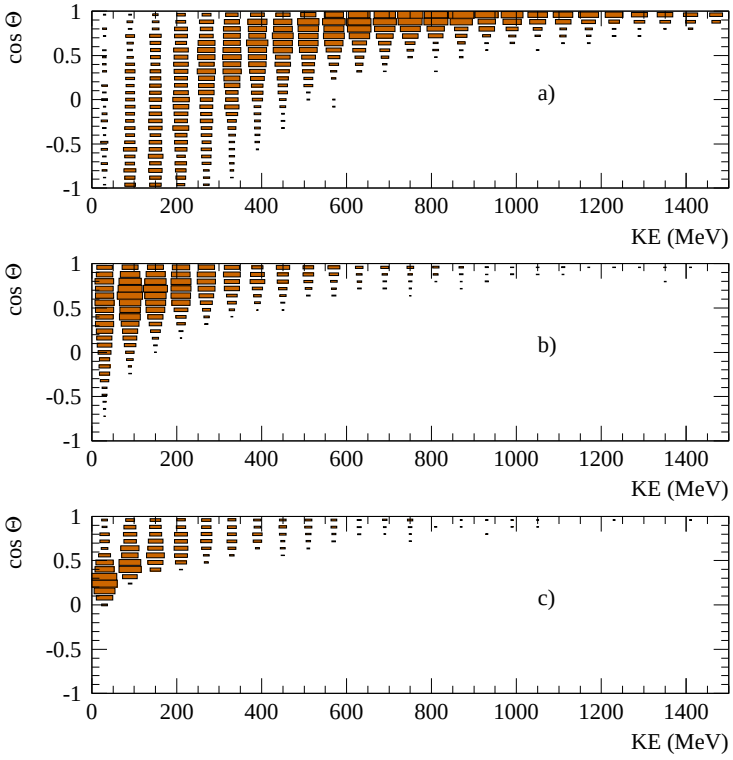

Figure 5.6: Kinetic energy vs. $\cos\theta$ for the a) μ, b) proton in CCQE scattering from bound nucleons, and c) proton in CCQE scattering from free nucleons. Protons in NCp reactions will show the same distribution as that in b).

The correlations shown in Fig. 5.6 will be used to reduce backgrounds from NC and CC single pion reactions by requiring that the reconstructed tracks obey the illustrated kinematic constraints.

5.2 Physics Simulations

The baseline detector, including the Vertex Detector and Muon Rangestack, has been simulated using the the GEANT3 [61] simulation package. Physics events were transported through this code, and the resulting simulated data reconstructed.

5.2.1 Simulation of the Detector

A diagram of the apparatus as modeled by the GEANT-based Monte Carlo program is shown in Fig. 5.7. The Vertex Detector is simulated as wavelength-shifting (WLS) fibers immersed in liquid scintillator with the same geometry as described in Section 4.2. The fiber support structure and tank walls are also included in the simulation. The area outside of the fiber area in the scintillator tank (the "veto") is active in the simulation. The Muon Rangestack, downstream of the Vertex Detector, is implemented with geometry as described in Section 4.3, which consists of alternating planes of scintillator and iron.

In the inner region of the Vertex Detector, scintillation light and Čerenkov radiation from passing charged particles are simulated. Photons thus produced are tracked until they impinge upon a WLS fiber or the edge of the detector volume, or are absorbed. In the outer 50 cm (veto) region of the liquid scintillator and in the Muon Rangestack, individual photons are not tracked – only energy loss is recorded. This is not important in these regions as photostatistics are not crucial.

In the active region of liquid scintillator, it is estimated that 5000 scintillation photons are produced in the liquid scintillator for every 1 MeV of energy deposited by a charged particle [56]. The absorption and capture efficiency of photons intersecting a WLS fiber is estimated to be 5% [56]. These fibers have typical attenuation lengths of 2.5 m, and the quantum efficiency of the PMT is approximately 20%. As a result, approximately 10% of the photons emitted in the capture cone of the fiber will make it to the PMT and produce a photoelectron. Combining these two factors yields an overall efficiency of 0.5% that an optical scintillation photon that strikes a WLS

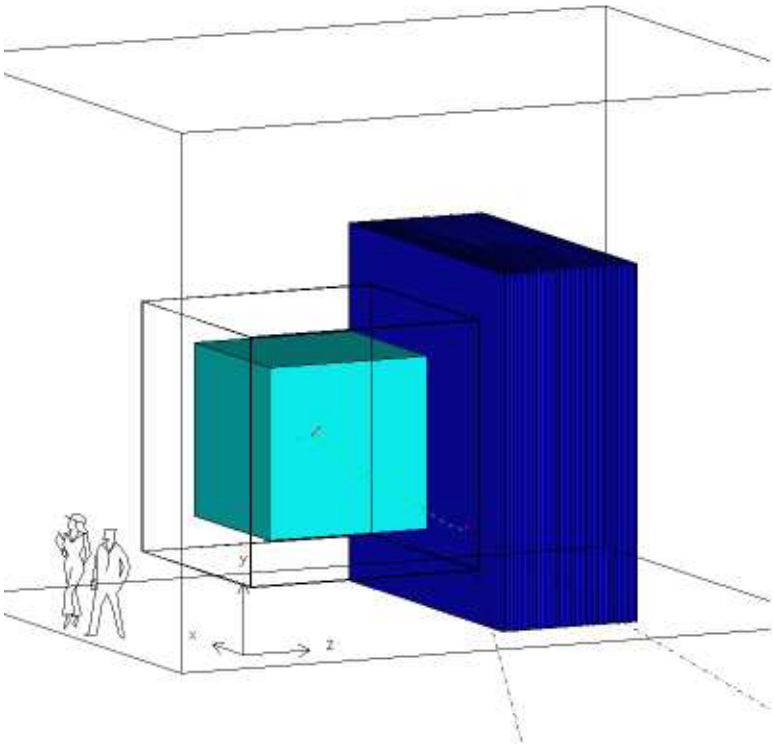

Figure 5.7: Diagram of the detector geometry as simulated by GEANT with a superimposed CCQE scattering event.

fiber will be detected at the PMT. To aid the speed of the simulation, the photon detection efficiency and production was combined so that 25 (5000×0.005) photons are produced per MeV. An effective efficiency of 100% for the photons that hit a 1.5 mm WLS fiber was then assumed. In this way, the effects of photostatistics were properly simulated and the efficiency of the simulation was kept high. The attenuation length (5 m) [56] of the scintillator is fairly large compared to the size of the detector and is not a significant effect. The saturation due to large localized energy deposits ("Birks' Law") is also modeled. The production of Čerenkov photons is simulated but is negligible as the number of Čerenkov photons is only about 1% of that for scintillation.

Using these factors, the simulation predicts that a proton track passing near a fiber will create, on average, 10 photoelectrons in the PMT. This is consistent with the earlier prototype test results reported in Chapter 4 (factoring in the difference in fiber length). Recent tests indicate that this number may be made higher with an optimal fiber/scintillator combination. Employing this method of tracking individual optical photons in the Vertex Detector assures that the photo statistics (with fluctuations) are properly simulated.

The simulation program can track single-particle events to study the detector response for each particle type. Alternatively, it can accept event descriptions as generated by the NUANCE MC program as described in Chapter 3. The latter class are events that are used to predict physics sensitivities. The output of the detector simulation includes: a list of all the "hit" fibers in the Vertex Detector, a list of all the bars in the Muon Rangestack that recorded energy loss, and the total amount of energy and time of deposit in each area of the detector. These data are subsequently passed through the event reconstruction program.

5.2.2 Event Reconstruction

The Monte Carlo simulation sample with the Vertex Detector is analyzed with a reconstruction program employing the Hough Transformation Technique (HTT) [62]. The HTT transformation is a global track finding method that uses the hit fiber information from the XZ and YZ orientations (The information from the XY orientation has not yet been used — this information will improve the reconstruction from what is reported here). The coordinates of each fiber that record an amount of light over an

adjustable threshold value are used to calculate R, the perpendicular distance from the track to the origin:

$$R = X(Y)\sin\alpha + Z\cos\alpha \ , \tag{5.1}$$

where α is a track angle. The track angle α is varied in a loop from $-90°$ to $+90°$, and the R and α values for each hit are used to make an entry (weighted by the amount of light in the hit) in a histogram.

The task of track finding then reduces to locating "peaks" in this histogram. Locating single tracks is quite easy with this method. For events with multiple tracks, alternate methods have been developed and tuned to subtract the light from the first track before the algorithm is employed to find subsequent tracks. At present, the reconstruction program is limited to finding a maximum of two tracks in each of the two 2D-orientations (XZ, YZ).

The 2D-tracks are then combined to form 3D-tracks. The total energy and length of each track are also calculated, from which the dE/dx of the track can be determined.

The simulated detector energy, angle, and position resolutions for 50-500 MeV kinetic energy (KE) protons and muons are shown in Figure 5.8. This energy range is typical for the tracks that will be contained in the Vertex Detector for physics events. This proton kinetic energy range corresponds to Q^2 values ranging from 0.1-1.0 GeV^2 in NCp and CCQE reactions. A Gaussian fit to the energy and angle resolution yields $\Delta E = 13(16)$ MeV and $\Delta\theta = 100(80)$ mrad for protons (muons). The quantity Δv plotted in Figure 5.8 is the distance from the calculated track origin from the true origin. The simulations of single particles predict a mean $\Delta v = 9(10)$ cm for protons (muons). The distribution is slightly wider for muons as they produce longer tracks. These results indicate detector performance that will meet the physics goals of the experiment. The effect of the detector resolution on the physics distributions will be shown in the following sections.

Several examples of the tracks obtained with the HTT reconstruction method from simulated data are shown in Figures 5.9 and 5.10. In these figures, the particle directions are indicated by the red(light) arrows. The reconstructed tracks and endpoints are indicated by blue(dark) lines and dots. As indicated, this method results in accurate reconstructed tracks for muons and protons down to kinetic energies of 100 MeV.

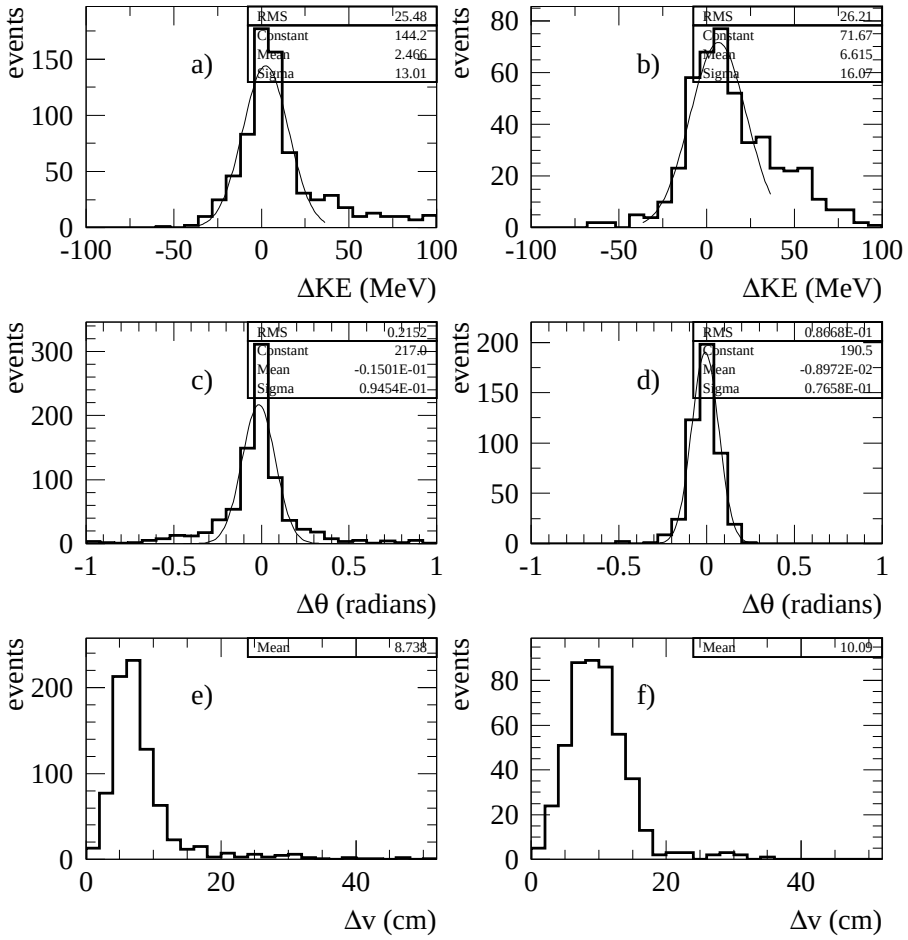

Figure 5.8: The energy a,b), angle c,d), and position e,f) resolution of the Vertex Detector as simulated and reconstructed for a sample of 1000 single particle events. The plots on the left a,c,e) are for 50-500 MeV KE protons, those on the right b,d,f) for 50-500 MeV KE muons. Only tracks that were fully contained in the Vertex Detector were selected. This effectively limits the upper muon KE to ≈ 300 MeV.

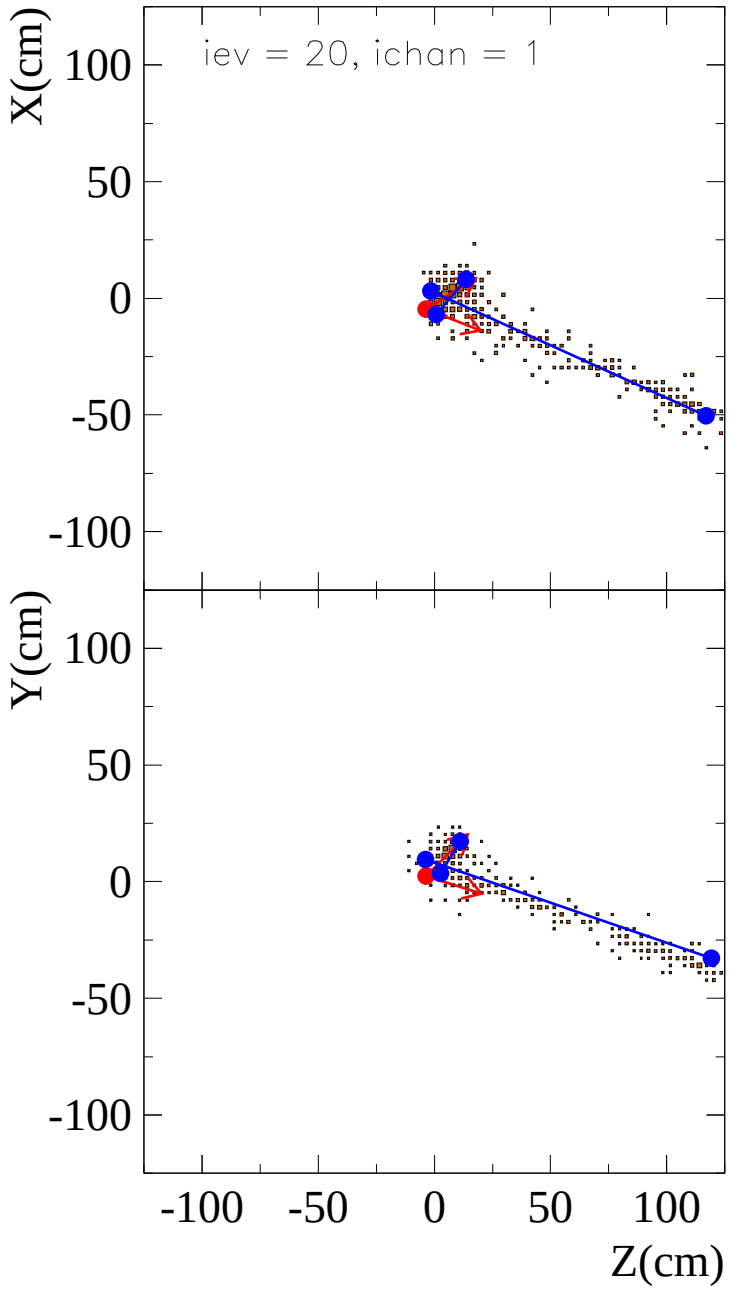

Figure 5.9: A XZ (top) and YZ (bottom) projection view of a CCQE event in the simulated Vertex Detector with the reconstructed muon (long line) and proton (short line) tracks superimposed. In this event, $T_\mu = 820$ MeV and $T_p = 150$ MeV.

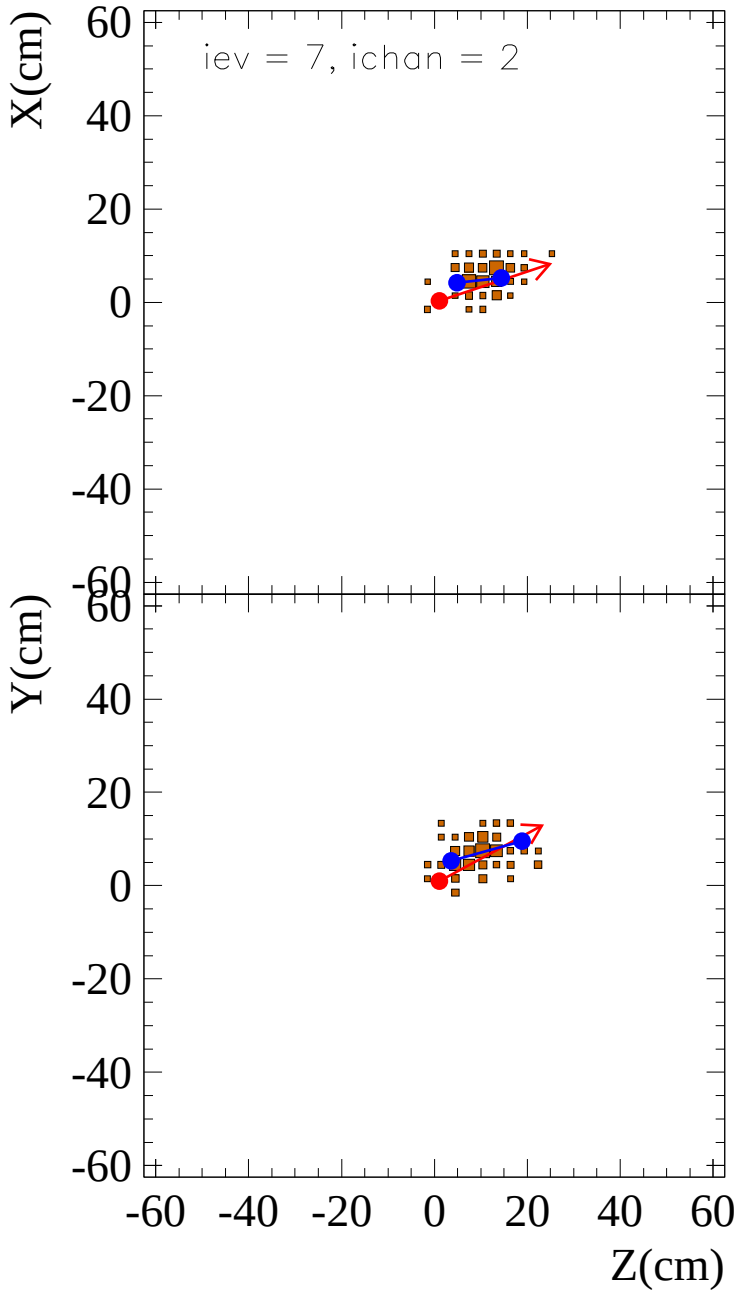

Figure 5.10: A XZ (top) and YZ (bottom) projection view of a NCp event in the simulated Vertex Detector with the reconstructed proton track superimposed. In this event, $T_p = 100$ MeV.

5.3 Physics Sensitivities

5.3.1 Δs Measurement

To extract Δs from the data, the ratio,

$$R_{NC/CC} = \frac{\sigma(\nu p \to \nu p)}{\sigma(\nu n \to \mu^- p)}, \tag{5.2}$$

will be employed. To form this ratio from the experimental data, neutral-current elastic scattering events ($\nu p \to \nu p$) and charged-current quasi-elastic scattering events ($\nu n \to \mu^- p$) will be identified, counted, and corrected for experimental efficiencies.

Both Neutral-current elastic and Charged-current quasi-elastic events have unique final state signatures. Neutral-current elastic scattering events (NCp) will be identified in the detector by looking for single proton tracks consistent with elastic scattering kinematics. A track is identified as a proton by a large dE/dx. Charged-current quasi-elastic scattering events (CCQE) are identified by looking for events with two tracks each consistent with the expected dE/dx. In addition, other cuts are employed to reject backgrounds. The strategy will be to maintain a compromise between large efficiency for low-Q^2 events while keeping backgrounds as low as possible. The squared four-momentum transfer, Q^2, will be determined event by event, by measuring the energy of the proton in both NC and CC events. Q^2 is determined from the energy via $Q^2 = 2m_p T_p$.

This strategy has been developed and tested using the GEANT3 Monte Carlo simulation of the detector and event reconstruction program as described above. A large sample of physics events with vertices evenly distributed within the nominal volume of the Vertex Detector $(2.4\ \mathrm{m})^3$ were tracked through the detector simulation. This event sample included both signal and background events as modeled by the NUANCE Monte Carlo [54]. The event types and relative frequencies are shown in Table 3.1.

The results from this exercise are summarized in Table 5.2. The efficiencies and Q^2 resolutions for the NCp and CCQE signal samples are shown in Figures 5.11 and 5.12. Note the large efficiency for reconstructing NCp, and reasonable efficiency for CCQE, in the $Q^2 = 0.2 - 0.4\ \mathrm{GeV}^2$ region. At low Q^2, proton tracks from NCp are short and difficult to reconstruct, causing a fall off in the efficiency. At high Q^2, final state particles tend not to be contained for both the NCp and CCQE samples,

causing a fall of the efficiency in these regions also. In addition to this, very forward events in the NCp sample are cut to remove backgrounds from pions. This further decreases the NCp efficiency at high Q^2.

	reaction channel				
NCp cuts	NCp	NCn	NCπ	CCQE	CCπ
raw events	21219	20487	19062	100102	54107
passed events	3929	1162	167	48	4
efficiency (%)	18.5	5.7	0.9	0.0	0.0
fid. eff. (%)	27.1	8.3	1.3	0.1	0.0
purity (%)	74.0	21.9	3.1	0.9	0.1
CCQE cuts	NCp	NCn	NCπ	CCQE	CCπ
raw events	21219	20487	19062	100102	54107
passed events	165	76	581	7323	1322
efficiency (%)	0.8	0.4	3.0	7.3	2.4
fid. eff. (%)	1.1	0.5	4.5	10.6	3.6
purity (%)	1.7	0.8	6.1	77.4	14.0

Table 5.2: Summary of events that passed the NCp and CCQE cuts along with efficiencies and purities: "efficiency" is the reconstruction efficiency throughout the $(2.4\ \mathrm{m})^3$ volume. "fid. eff." is the reconstruction efficiency within the $(2.2\ \mathrm{m})^3$ fiducial volume. The simulation data set contained 215k events which is the sum of the raw events across the 5 columns plus a small number of νe elastic scattering events.

Using these reconstructed events, $G_A^s(Q^2 = 0)$ $(=\Delta s)$, was calculated for the simulated data set and its sensitivity to various experimental and errors was determined. The errors considered in this procedure include:

1. statistics of event samples;
2. neutrino backgrounds;
3. scattering from free protons in CH_2;
4. experimental systematics in calculated efficiencies and Q^2 reconstruction;
5. systematics due to uncertainties in backgrounds;
6. nuclear model uncertainties;

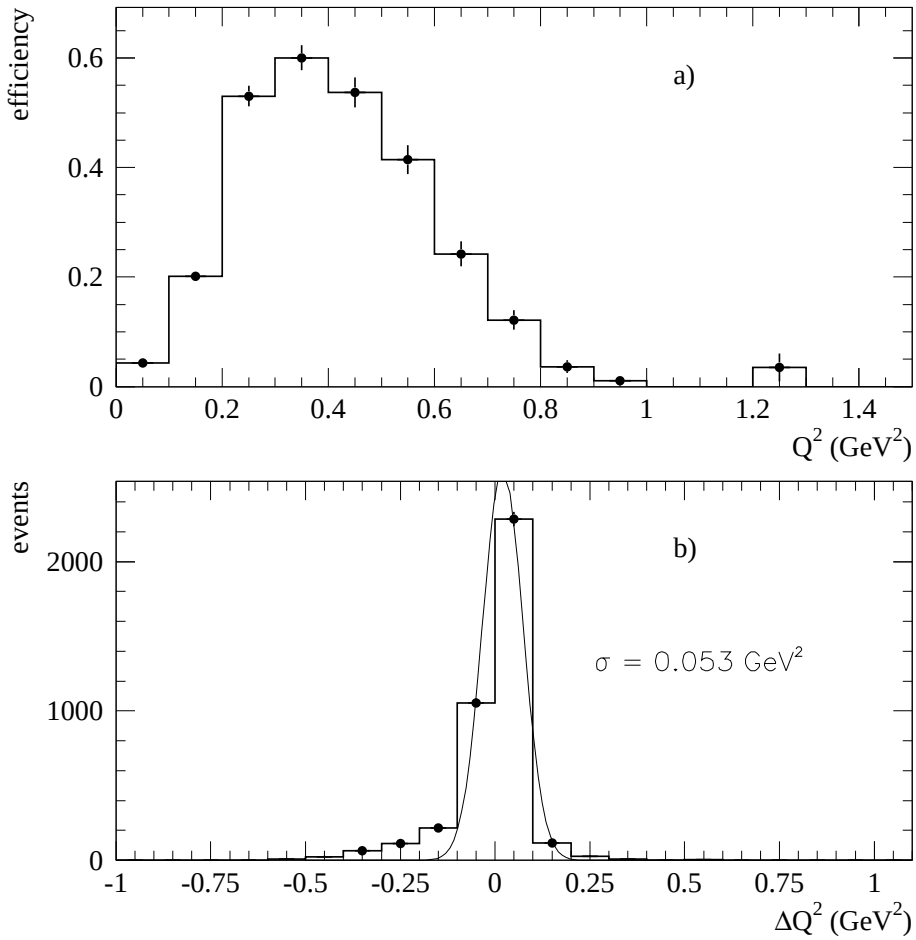

Figure 5.11: a) Efficiency for reconstructing true NCp events with the NCp cuts within the fiducial volume as a function of generated Q^2 and b) the distribution of the difference between generated and reconstructed Q^2 for this sample. The σ of this distribution is 0.053 GeV^2.

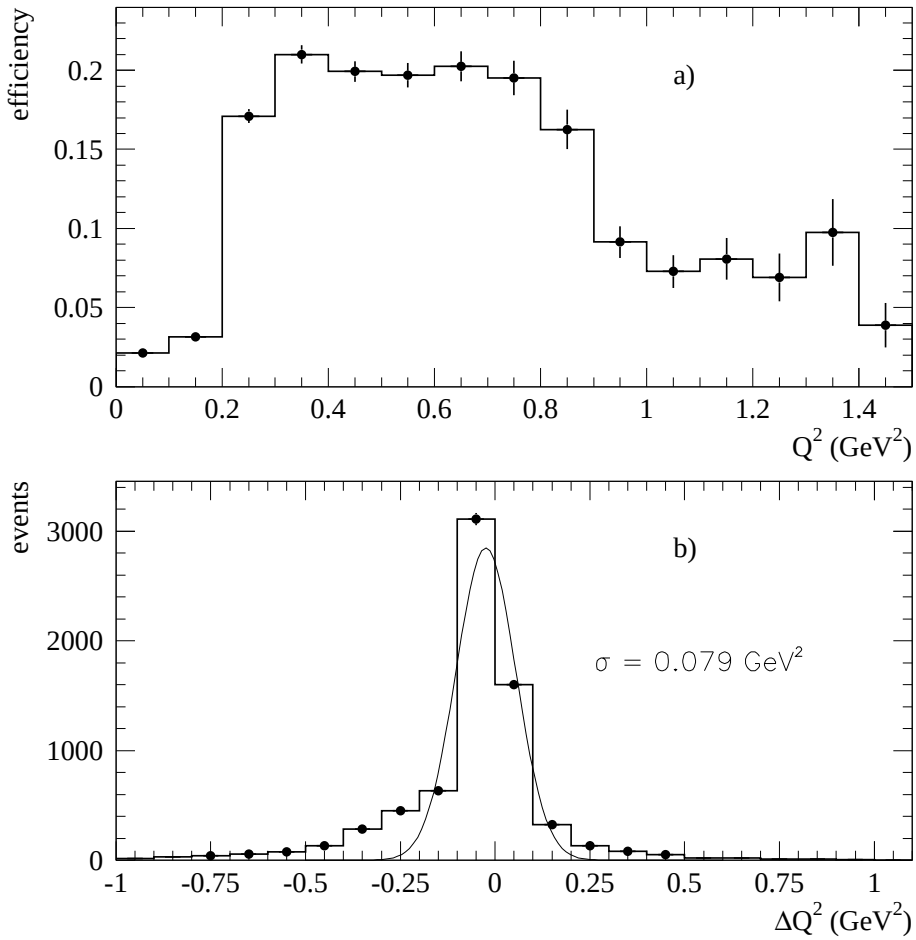

Figure 5.12: a) Efficiency for reconstructing true CCQE events with the CCQE cuts within the fiducial volume as a function of generated Q^2 and b) the distribution of the difference between generated and reconstructed Q^2 for this sample. The σ of this distribution is 0.079 GeV^2.

7. and form factor uncertainties.

With fairly conservative assumptions for all of these error contributions, the uncertainty on G_A^s from this simulated data set was determined to be ± 0.04 due to all errors except form factor uncertainties.

At present, form factor uncertainties introduce an additional ± 0.025 error which would be added in quadrature. However it is likely this will be reduced with a combined fit procedure to new neutrino and electron scattering data as described in Chapter 2. It is for this reason that we list these errors separately.

The dominant contributions to the form factor uncertainties come from the uncertainty in the axial vector mass, M_A, and from the isoscalar part of the vector form factor, F_2^s. The sensitivity of the G_A^s result to these two form factor parameters may be seen in Figure 5.13. The current world average of M_A as measured in neutrino scattering is 1.026 ± 0.021 GeV [17]. This uncertainty adds approximately 0.015 to the uncertainty in G_A^s. The sensitivity of G_A^s on F_2^s is weaker, but this form factor is not well known directly. Linear combinations of this form factor with F_1^s have been measured [29]. A conservative estimate on the uncertainty on F_2^s is ± 0.1. An uncertainty of this size in F_2^s will contribute an uncertainty of ± 0.02 to G_A^s. Combining these yields a ± 0.025 uncertainty on G_A^s, which is what we presently quote, but expect to see reduced in in the future.

Work is ongoing to reduce the remaining ± 0.04 error. The largest contributor to this is the background from $\nu n \to \nu n$ events in the $\nu p \to \nu p$ signal as can be seen in Table 5.2. This background is the most problematic because the rate of $\nu n \to \nu n$ also depends upon G_A^s in a way that dilutes the sensitivity of $R_{NC/CC}$ to G_A^s. It is likely that this contribution can be reduced substantially with a scheme to identify neutron capture photons. This technique is not used in the reconstruction utilized to date.

5.3.2 Neutrino Cross Section Measurements

As demonstrated in the preceding discussion, the CCQE and NC channels can be easily reconstructed and isolated because of their simple event topologies. Making further use of the superior detector resolution and final state particle identification made available by this fine-grained detector technology, more complicated multi-track

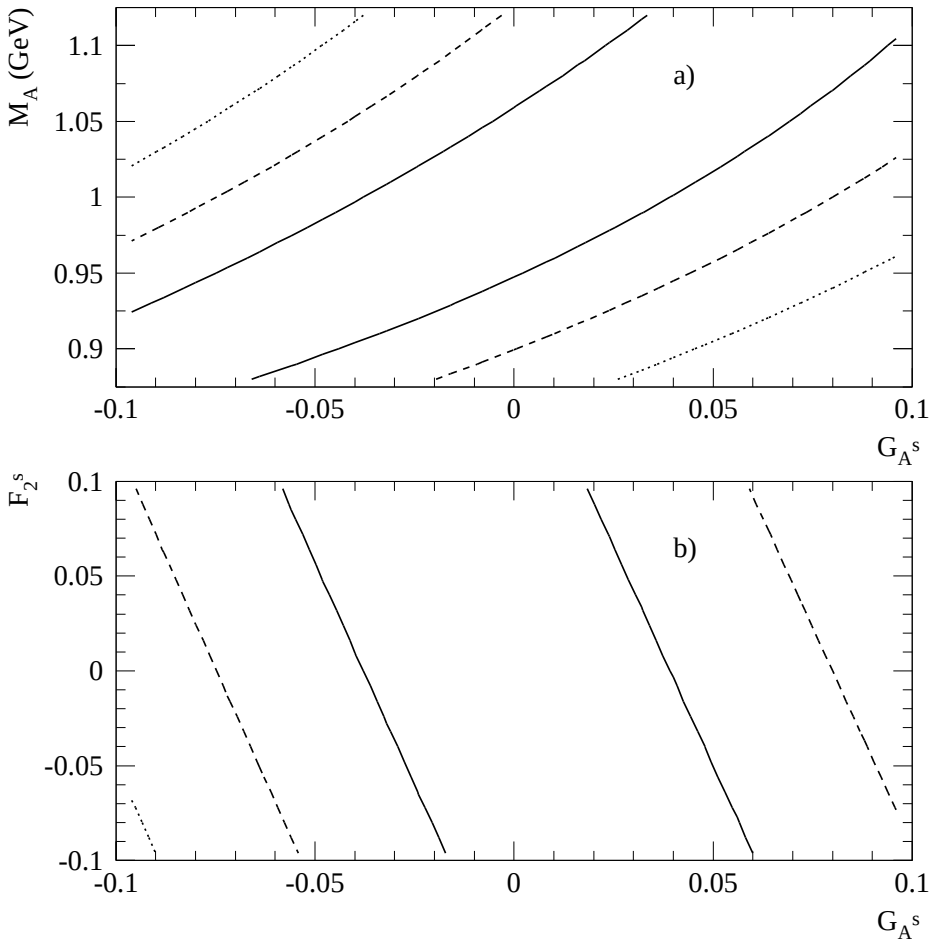

Figure 5.13: χ^2 contours corresponding to 1σ (solid), 2σ (dashed), and 3σ (dotted) resulting from the a fit procedure to extract G_A^s from the simulated data set. In a) G_A^s and M_A, the axial vector mass, are varied, in b) G_A^s and F_2^s are varied. In these plots G_A^s and F_2^s are the $Q^2 = 0$ values of these form factors.

events can also be more readily identified. This includes both NC and CC resonant interactions producing a pion or kaon in the final state.

Single Neutral Pion Measurements

Over the course of the four month run proposed here, the experiment would accumulate a total sample of $\sim 15,000$ NC π^0 resonant events and $\sim 5,000$ NC coherent π^0 interactions. The superior event reconstruction capabilities of the proposed Vertex Detector would greatly enhance the ability to select π^0 interactions beyond that which is achievable in large open volume Čerenkov based detectors in present use. A $\nu_\mu p \rightarrow \nu_\mu p \pi^0$ interaction (Figure 5.14) can be distinguished by the presence of three isolated energy deposition clusters corresponding to the final state proton and the two photons emitted from the $\pi^0 \rightarrow \gamma\gamma$ decay. A charged current π^0 event, $\nu_\mu n \rightarrow \mu^- p \pi^0$, (Figure 5.15) is additionally accompanied by a final state muon track. NC coherent π^0 events (Figure 5.16) are similar in signature to the former class of events; but, in this case, the energies and angles of the two final state photons can be used to determine if the π^0 angular distribution is more forward peaked as one expects for coherent scattering.

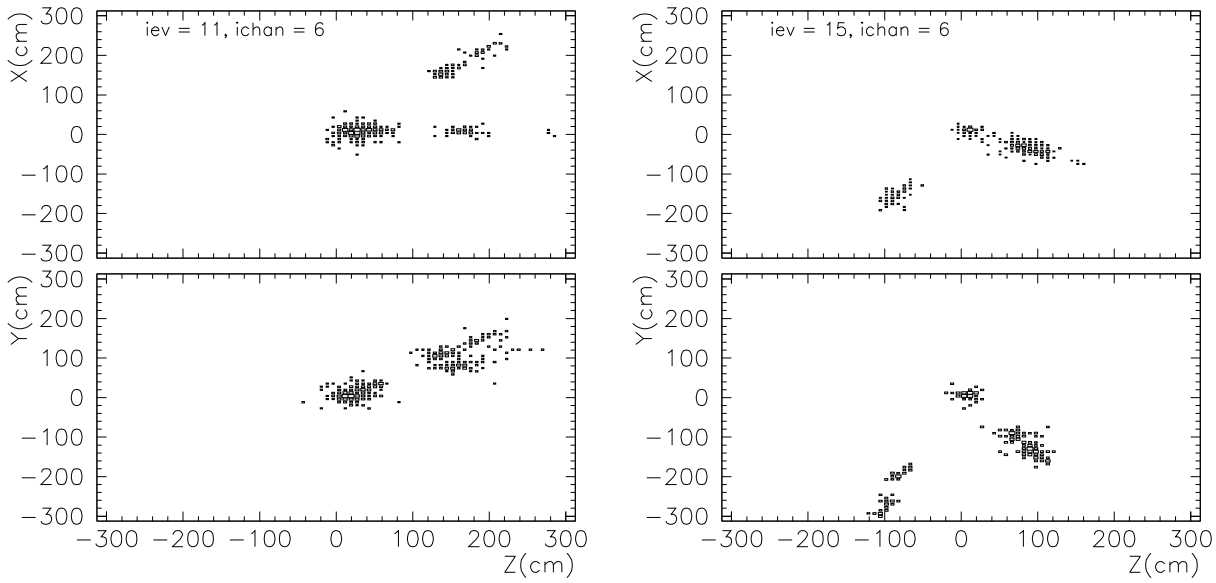

Figure 5.14: Hit-level simulations of NC π^0 interactions in the Vertex Detector, $\nu_\mu p \rightarrow \nu_\mu p \pi^0$. The three hit clusters correspond to the final state proton and two photons from $\pi^0 \rightarrow \gamma\gamma$.

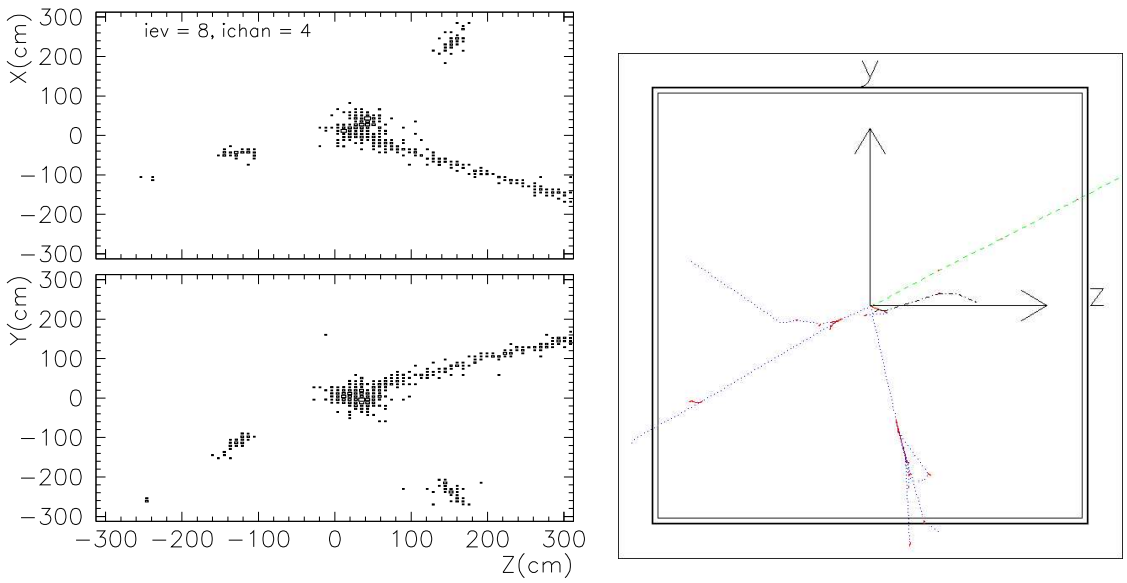

Figure 5.15: A CC π^0 interaction in the Vertex Detector, $\nu_\mu n \rightarrow \mu^- p \pi^0$ The right hand figure shows the true GEANT particle trajectories in the YZ plane. In this case, a muon is produced in addition to the three hit clusters from the proton and two photons.

Although such events leave distinct signatures in the Vertex detector, determining the efficiency and accuracy with which the detector can measure π^0 rates and kinematics will require development of a cluster algorithm and tracker designed to locate gaps in energy deposits. While not yet optimized, preliminary studies indicate that π^0 efficiencies and purities can be obtained that surpass those achieved with either the MiniBooNE or K2K Čerenkov–based detectors.

Single Kaon Production

Based on NUANCE Monte Carlo predictions, more than a hundred single kaon interactions are expected in four months of running. If such kaon events can be isolated, this experiment will provide crucial new information to proton decay searches not only because of potentially large event samples, but also because these interactions will be taking place at energies near threshold and on a nuclear target. Identifying such events will certainly be challenging. Although the event signature is complex, it is potentially very distinctive. Roughly 64% of the time, a typical CC kaon event will contain two oppositely charged muons, one from the primary neutrino interaction and

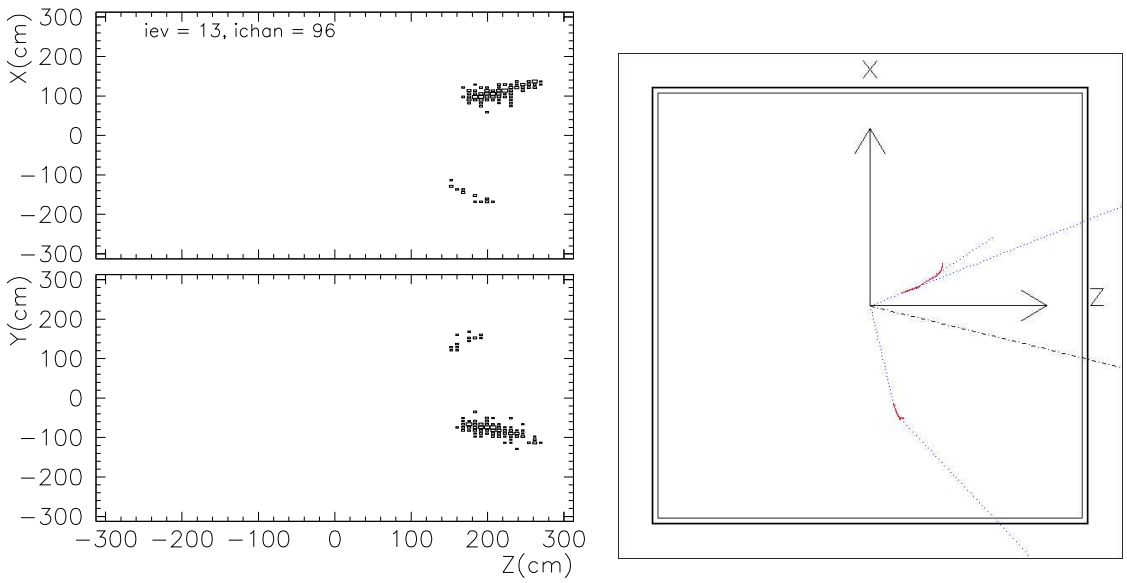

Figure 5.16: A NC coherent π^0 interaction in the Vertex Detector, $\nu_\mu\,{}^{12}C \rightarrow \nu_\mu\,{}^{12}C\,\pi^0$. The figure on the right shows the true GEANT particle trajectories in the XZ plane for the same event. As can be seen, the hit clusters correspond to the two photons from the π^0 decay.

the other from the K decay, $K^+ \rightarrow \mu^+\nu_\mu$ (Figure 5.17). In addition, since most of the kaons will stop and decay at rest, the μ^+ is mono-energetic with a momentum of ~ 240 MeV, and will appear roughly 12 ns after the initial interaction. Such a signature should be easy to separate from resonant pion interactions and more complicated DIS events.

Further studies must assess the Vertex Detector's multi-track reconstruction capabilities and DIS backgrounds before any stringent limits on strange particle production can be set. We believe such a possibility should be seriously explored as this experiment could potentially be the first to measure this reaction both near threshold and on a nuclear target.

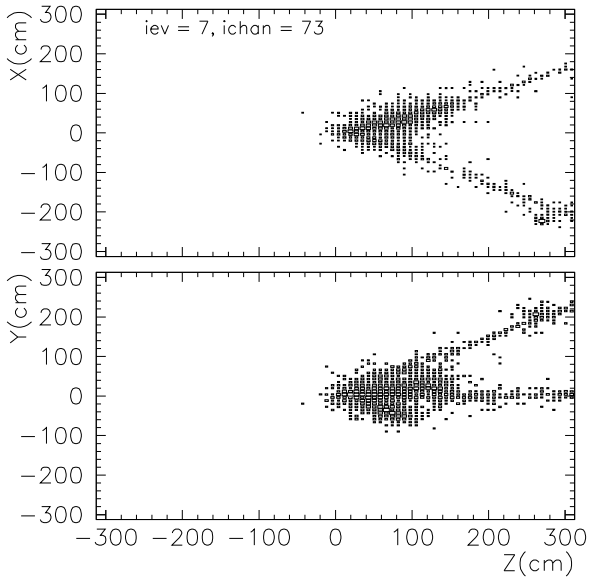

Figure 5.17: Example of a $\nu_\mu\, n \rightarrow \mu^-\, K^+\, \Lambda$ event in the Vertex Detector. In this event, the associated strange particles decayed yielding a hadronic shower and second muon: $\Lambda \rightarrow p\,\pi^-$ (BR=63%) and $K^+ \rightarrow \mu^+ \nu_\mu$ (BR=64%).

Chapter 6

Conclusions

In this letter, we have put forth the case to build a small neutrino experiment at Brookhaven to measure the strange-quark contribution to the nucleon spin as well as important neutrino interaction cross sections.

Determination of the strange spin of the proton, Δs, as described here, uses a theoretically robust method; an intense, low-energy neutrino beam; and a novel detection technique. With this experiment and the existing RHIC spin physics program, Brookhaven comprehensively measures the spin carried by all the light sea quarks and the gluons in the nucleon.

Measurements of neutrino cross sections in this energy range are crucial for future oscillation measurements as well as for our understanding of neutrino interactions. To further advance this knowledge, this experiment combines for the first time a high-statistics data sample with fine-grained detection capabilities.

This experiment can be mounted quickly and relatively inexpensively. A new neutrino beamline, built in the existing U-Line, would provide the world's highest intensity neutrino beam in the 0.5-1.0 GeV neutrino energy range. With a high intensity AGS beam running concurrently with the RHIC program, the experiment can be performed over a short 4 month run, with a relatively simple and small, 9 ton fiducial volume, detector.

Based on this, we plan to submit a proposal for this experiment to the Brookhaven directorate in 2005. We look forward to comments and encouragement from the Brookhaven PAC regarding this Letter of Intent. Thank you for your consideration.

Bibliography

[1] L. A. Ahrens *et al.*, Phys. Rev. **D35**, 785 (1987).

[2] B. W. Filippone and X. D. Ji, Adv. Nucl. Phys. **26**, 1 (2001), hep-ph/0101224.

[3] S. J. Brodsky *et al.*, Phys. Lett. **B206**, 309 (1988).

[4] S. D. Bass, hep-ph/0311174; S. D. Bass and A. W. Thomas, hep-ph/9310306.

[5] S. L. Adler, Phys. Rev. **177**, 2426 (1969); J. S. Bell and R. Jackiw, Nuovo Cimento **60A**, 47 (1969).

[6] S.-L. Zhu *et al.*, Phys. Rev. **D66** 034021 (2002).

[7] R. Buras, M. Rampp, H.-Th Janka, K. Kifonidis, PRL **90** (2003) 241101.

[8] C. J. Horowitz, PRD **65** (2002) 043001.

[9] J.R. Ellis, A. Ferstl and K.A. Olive, "Theoretical aspects of dark matter detection,",hep-ph/0106148.

[10] K. A. Olive, hep-ph/0308035.

[11] V. Barger *et al.*, Phys. Rev. **D65**, 075022 (2002).

[12] B. Adeva *et al.*, Phys. Lett. **B412**, 414 (1997).

[13] See, for example: V. A. Bednyakov, hep-ph/0310041.

[14] L. A. Ahrens *et al.*, Phys. Rev. **D34**, 75 (1986).

[15] N. Baker *et al.*, Phys. Rev. **D23**, 2499 (1982); K. Miller *et al., ibid.* **26**, 537 (1982); T. Kitagaki *et al., ibid.* **28**, 436 (1983).

[16] G. Garvey *et al.*, Phys. Rev. **C48**, 761 (1993).

[17] V. Bernard et al., J. Phys. G: Nucl. Part. Phys. **28** R1 (2002), hep-ph/107088.

[18] W. M. Alberico *et al.*, Nucl. Phys. **A651**, 277 (1999).

[19] K. Ackerstaff *et al.* Nucl. Instrum. Meth. A **417**, 230 (1998), arXiv:hep-ex/9806008.

[20] A. Airapetian *et al.*, Phys. Rev. Lett. **92**, 012005 (2004), arXiv:hep-ex/0307064.

[21] J. Pumplin *et al.*, JHEP **0207**, 012 (2002), hep-ph/0201195.

[22] M. J. Musolf *at al.*, Phys. Rep. **239**, 1 (1994).

[23] M. J. Musolf and B. R. Holstein, Phys. Lett. **B242**, 461 (1990).

[24] M. J. Musolf and T. W. Donnelly, Nucl. Phys. **A546**, 509 (1992).

[25] S.-L. Zhu *et al.*, Phys. Rev. **D66**, 034021 (2002).

[26] D. T. Spayde *et al.*, Phys. Lett. **B583**, 79 (2004); T. M. Ito *et al.*, Phys. Rev. Lett. **92**, 102003 (2004).

[27] The COMPASS Experiment, `http://wwwcompass.cern.ch/`, Alain Magnon and Gerhard Mallot, spokespersons.

[28] S. F. Pate, Phys. Rev. Lett. **92**, 082002 (2004).

[29] K. A. Aniol *et al.*, Phys. Lett. **B509**, 211 (2001).

[30] G^0 Experiment, `http://www.npl.uiuc.edu/exp/G0/`, Doug Beck, spokesperson.

[31] P. Lipari, Nucl. Phys. Proc. Suppl. **112**, 274 (2002).

[32] A. Suzuki *et al.*, Nucl. Instr. Meth. **A453**, 165 (2000); T. Ishii *et al.*, Nucl. Instr. Meth. **A482**, 244 (2002).

[33] T. Ishida, Nucl. Proc. Suppl. **112**, 132 (2002); C. Mauger, Nucl. Phys. Proc. Suppl. **112**, 146 (2002); C. W. Walter, Nucl. Phys. Proc. Suppl. **112**, 140 (2002).

[34] D. Rein and L. M. Sehgal, Annals Phys **133**, 79 (1981).

[35] D. Casper, Nucl. Phys. Proc. Suppl. **112**, 161 (2002); H. Gallagher, Nucl. Proc. Suppl. **112**, 188 (2002).

[36] E. Hawker, "Single Pion Production in Low Energy Neutrino-Carbon Interactions", NuInt02 workshop proceedings, to appear in Nucl. Proc. Suppl. (2004).

[37] P. Vilain *et al.*, Phys. Lett. **313B**, 267 (1993).

[38] H. Faissner *et al.*, Phys. Lett. **125B**, 230 (1983).

[39] E. A. Paschos and A. V. Kartavtsev, hep-ph/0309148; J. Marteau *et al.*,hep-ph/9906449.

[40] D. Rein and L. M. Sehgal, Nucl. Phys. **B223**, 29 (1983).

[41] Y. Hayato, "K2K Near Detector Upgrade", NuInt02 workshop proceedings, to appear in Nucl. Proc. Suppl. (2004).

[42] W. A. Mann *et al.*, Phys. Rev. **D34**, 2545 (1986).

[43] R. E. Shrock, Phys. Rev. **D12**, 2049 (1975); A. A. Amer, Phys. Rev. **D18**, 2290 (1978).

[44] http://www.interactions.org/cms/?pid=1011988

[45] G. Danby, J. M. Gaillard, K. Goulianos, L. M. Lederman, N. Mistry, M. Schwartz and J. Steinberger, "Observation Of High-Energy Neutrino Reactions And The Existence Of Two Kinds Of Neutrinos," Phys. Rev. Lett. **9**, 36 (1962).

[46] M. V. Diwan *et al.*, "Very long baseline neutrino oscillation experiments for precise measurements of mixing parameters and CP violating effects," Phys. Rev. D **68**, 012002 (2003), hep-ph/0303081.

[47] J. W. Glenn, T. Roser, and P. Pile. private communication.

[48] E. Church *et al.* [BooNe Collaboration], "A proposal for an experiment to measure muon-neutrino $\rightarrow$ electron-neutrino oscillations and muon-neutrino disappearance at the Fermilab Booster: BooNE," FERMILAB-PROPOSAL-0898, http://www.slac.stanford.edu/spires/find/hep/www?r=fermilab-proposal-0898.

[49] *"Technical Design Report for the Primary Beam.* The MiniBooNE collaboration: http://www-boone.fnal.gov/publicpages/index.html.

[50] A. A. Aguilar-Arevalo *et al.*, "The MiniBooNE Run Plan", October 2003.

[51] I. Chemakin *et al.*, Phys. Rev. **C65**, 024904 (2002), nucl-ex/0108007.

[52] HARP collaboration, Status Report to SPSC, CERN-SPSC/2003-027, August 2003.

[53] M. Sorel, "Error on the MiniBooNE Neutrino Flux Arising from Finite HARP Statistics", MiniBooNE memo, August 2002.

[54] D. Casper, Nucl. Phys. Proc. Suppl. **112**, 161 (2002).

[55] K. Nitta, *et al.*, "The K2K Scibar Detector", hep-ex/0406023.

[56] Saint-Gobain Crystals and Detectors, Newbury, OH 44065-9677, http://www.detectors.saint-gobain.com.

[57] http://usa.hamamatsu.com/.

[58] C.E. Allgower *et al.*, Nucl. Instrum. Meth. **A 499**, 740 (2003).

[59] Arneodo *et al.*, "Observation of long ionizing tracks with the ICARUS T600 first half-module," Nucl. Instrum. Meth. A **508**, 287 (2003) [Erratum-ibid. A **516**, 610 (2004)].

[60] Flavio Cavanna, private communication.

[61] R. Brun, R. Hagelberg, M. Hansroul and J. C. Lassalle, "Geant: Simulation Program For Particle Physics Experiments. User Guide And Reference Manual," CERN-DD-78-2-REV.

[62] P. V. C. Hough, "Machine Analysis of Bubble Chamber Pictures", *International Conference on High Energy Accelerators and Instrumentation*, CERN, (1959).